BB

LBL-36731
UC-413
Preprint

Lawrence Berkeley Laboratory
UNIVERSITY OF CALIFORNIA

Submitted to Physical Review C

Heavy Residues from Very Mass Asymmetric Heavy Ion Reactions

K.A. Hanold, D. Bazin, M.F. Mohar, L.G. Moretto,
D.J. Morrissey, N.A. Orr, B.M. Sherrill, J.A. Winger,
G.J. Wozniak, and S.J. Yennello

January 1995

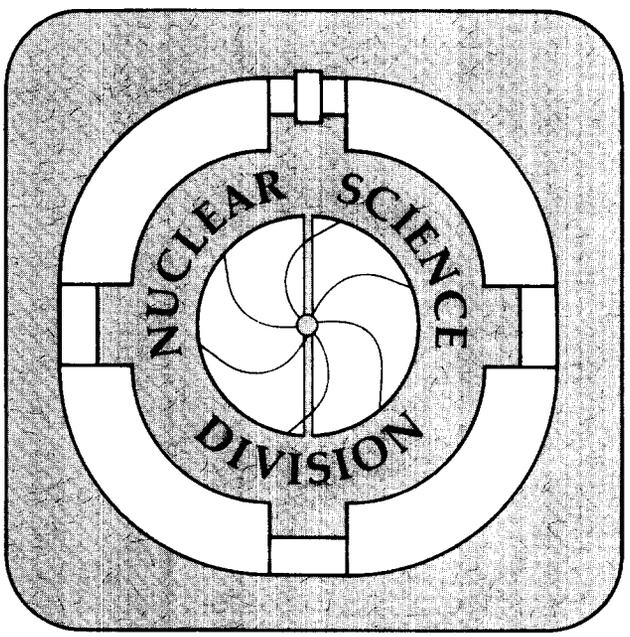

Prepared for the U.S. Department of Energy under Contract Number DE-AC03-76SF00098

LBL - 36731
UC 413

HEAVY RESIDUES FROM VERY MASS ASYMMETRIC HEAVY ION REACTIONS

K.A. Hanold[a], D. Bazin[b], M.F. Mohar[b], L.G. Moretto[a] D.J. Morrissey,[b,c] N.A. Orr[b], B.M. Sherrill[b,d], J.A. Winger,[b] G.J. Wozniak[a], and S.J. Yennello[b]

[a] *Lawrence Berkeley Laboratory, University of California, Berkeley, CA 94720*

[b] *NSCL, Michigan State University, East Lansing, MI 48824*

[c] *Department of Chemistry, Michigan State University, East Lansing, MI 48824*

[d] *Department of Physics, Michigan State University, East Lansing, MI 48824*

January 1995

This work was supported by the Director, Office of Energy Research Division of Nuclear Physics of the Office of High Energy and Nuclear Physics of the U.S. Department of Energy under Contract DE-AC03-76SF00098

HEAVY RESIDUES FROM VERY MASS ASYMMETRIC HEAVY ION REACTIONS

K.A. Hanold[a,1], D. Bazin[b], M.F. Mohar[b,2], L.G. Moretto[a], D.J. Morrissey[b,c], N.A. Orr[b,3], B.M. Sherrill[b,d], J.A. Winger[b,4], G.J. Wozniak[a], and S.J. Yennello[b,5]

[a] *Lawrence Berkeley Laboratory, 1 Cyclotron Rd, Berkeley, CA 94720*
[b] *NSCL, Michigan State University, East Lansing, MI 48824*
[c] *Department of Chemistry, Michigan State University, East Lansing, MI 48824*
[d] *Department of Physics, Michigan State University, East Lansing, MI 48824*

ABSTRACT

The isotopic production cross sections and momenta of all residues with nuclear charge greater than 39 from the reaction of 26, 40, and 50 MeV/nucleon ^{129}Xe + Be, C, and Al were measured. The isotopic cross sections, the momentum distribution for each isotope, and the cross section as a function of nuclear charge and momentum are presented here. The new cross sections are consistent with previous measurements of the cross sections from similar reaction systems. The results are compared to a geometric incomplete fusion model and a Boltzman-Nordheim-Vlasov model. Agreement between the models and the data is fair. The most proton-rich nuclei observed in this study are predicted to have less than 50 nanobarn production cross sections by both of these models but are observed to have much larger cross sections.

Typeset using REVTEX

[1]Present address UCSD, Department of Chemistry-0314, 9500 Gilman Drive, La Jolla, CA, 92093-0314.
[2]Present address EG&G Energy Measurements, Washington Aerial Measurements Division, P.O. Box 380, Suitland, MD 20752.
[3]Present address LPC, Boulevard du Maréchal Juin, 14050 Caen Cedex, France.
[4]Present address Department of Physics and Astronomy, Mississippi State University, Mississippi State, Miss. 39762.
[5]Present address Cyclotron Institute, Texas A&M University, College Station, Texas, 77845-3366.

I. INTRODUCTION

The characterization of the source of complex fragments ($Z \geq 3$) in heavy ion induced reactions is presently of great interest. Complex fragment (CF) emission has been observed over a wide range of bombarding energies and combinations of projectile and target [1-36] CF data have been used as a tool to characterize the reaction mechanism of heavy ion reactions.

For asymmetric entrance channel reactions such as ^{139}La + C, studies have demonstrated the presence of a single source that emits complex fragments [17,37]. Information about this source was extracted from coincidence measurements of the complex fragments. The observed source velocity (v_{source}) was shown to be consistent with complete fusion at low beam energies ($E/A < 30$ MeV/nucleon) [17,38] and with incomplete fusion at higher beam energies ($E/A > 30$ MeV/nucleon) [26,36]. The center-of-mass angular distributions ($d\sigma/d\theta$) of the complex fragments were isotropic for a range of fragments with masses between the mass of the projectile and that of the target. These isotropic distributions result from the statistical decay of the fused product. The angular distributions of fragments with Z values near those of the projectile and target have both isotropic and anisotropic components. The anisotropic component results from the deep-inelastic process.

In contrast, more symmetric heavy ion collisions show a more complicated picture. The reaction of ^{139}La + Ni at 18 MeV/nucleon, for example, produces complex fragment velocity distributions that show no well-defined source [21]. The v_{source} from this reaction ranges from the velocity corresponding to complete fusion to near the velocity of the beam. By gating on the v_{source}, it was possible to characterize the mass and excitation energy of the compound nuclei formed in these incomplete fusion processes. This work was extended to higher bombarding energies for the ^{129}Xe + Ti and Cu reactions at 26 and 31 MeV/nucleon [38]. An incomplete fusion model calculation which incorporated statistical emission from the hot products reproduced the following experimental data: the elemental cross sections, the emission velocities of the decay products, the center-of-mass angular distributions, and the source velocity distributions.

At low excitation energies, however, complex fragment emission is quite rare. This implies that studies using complex fragments are ill suited to measure the yield of collisions that result in nuclei with low excitation energy. In the interpretation of ^{129}Xe+Ti and Cu and ^{139}La+Ti and Ni collisions, the authors claimed that the source velocity distribution was consistent with incomplete fusion processes; however, no events were observed with v_{source} above 90% of the velocity of the beam. The low-mass-transfer events populating this region were not observed because the product nuclei primarily de-excite via light particle evaporation and result in evaporation residues.

Since heavy residues result from compound nuclei with low excitation energy, they should be a good tool to study the small mass transfer limit of the incomplete fusion process. (In this discussion, compound nucleus will mean any hot nucleus that has distributed the excitation energy among all the available degrees of freedom.) Measurement of residue production resulting from incomplete fusion allows for the quantitative testing of the incomplete fusion model over the entire range of mass transfers. The studies mentioned above, which used a heavy projectile nucleus and a light target nucleus, were unable to detect fragments with Z values near that of the projectile. The detectors used in these studies were placed at angles larger than 30 mrad to avoid elastically scattered beam particles. The residues with Z values near that of the beam are kinematically constrained to small angles. (Typical laboratory frame emission angles for these residues are less than 30 mrad.)

For asymmetric heavy ion reactions at intermediate bombarding energies, the elemental cross sections for fragments with masses between those of the projectile and the light particles have been accounted for by a complete or incomplete fusion process followed by statistical de-excitation [38,26]. Although a systematic study of the cross sections has been carried out for fragments with masses between those of the light particles and the projectile [17,36–39], fragments with Z values near or above that of the projectile have not been measured because they are kinematically constrained to very small angles when using a heavy projectile and a light target. Since these heavy residues contain the bulk of the yield for very asymmetric entrance channels, only a small portion of the total reaction cross section

for these reactions has been measured. As a result, the model calculations that have been successful in predicting the complex fragment production have not been tested over the full range of Z values. In addition, since the isotopic distribution of the complex fragments has not been previously measured, the isotope production predictions of the models have not been tested.

In the present work, the production cross section for heavy residues from the reactions of 26, 40, and 50 MeV/nucleon ^{129}Xe + Be, C, and Al has been measured. To perform this measurement, a magnetic spectrometer was placed at 0 mrad in the laboratory frame and was used to measure the time of flight, the bend radius, the ΔE, and the total energy of each fragment produced in the reaction. The heavy residues were identified in Z and A. For each isotope, the absolute cross section and momentum distribution were determined.

This study provides a determination of the relative amounts of incomplete and complete fusion that is complementary to that obtained in the complex fragment studies. Events with very low excitation energy were easily measured since no fission-like decay was required. The isotopic yields were compared with the predicted yields from two models. Combining the present data with previous data, experimental cross sections spanning almost the entire range of Z values produced in these reactions have now been measured.

II. EXPERIMENTAL METHOD

The K1200 cyclotron at Michigan State University accelerated beams of ^{129}Xe ions to 26, 40 and 50 MeV/nucleon. The beam struck the target at 12 mrad with respect to the central axis of the A1200 spectrometer. The acceptance of the spectrometer, thus, ranged from 0 to 24 mrad in the laboratory frame and covered approximately 50% of the solid angle in this angular region. A schematic diagram of the A1200 spectrometer [40] is shown in Figure 1. The A1200 spectrometer consists of 14 superconducting quadrupoles and four superconducting dipoles. Four sextupoles are used for higher-order optical corrections. The A1200 spectrometer has an angular acceptance of 0.8 msr, 3% momentum acceptance, and

a maximum rigidity of 5.4 T-m.

In this study, the reaction products were identified with a technique similar to that used by Mohar et al. [41] and Bazin et al. [42]. This technique uses event-by-event measurements of the ΔE, the E_{total}, the time of flight, and the magnetic rigidity to give unambiguous isotope identification.

The ^{129}Xe beams bombarded targets of Be, C, and Al at the object point (labelled Target in Figure 1) of the A1200. The reaction products were collected and transported through the mass separator. At the first dispersive focus, labeled Image #1 in Figure 1, a gas multistep detector measured the position of each fragment. This detector also provided the start time for the time-of-flight measurement. The multistep detector was similar in design to a detector previously described by D.J. Vieira *et al.* [43]. The wire spacing in the detector was 1 mm, and the summed transparency for all wire planes was better than 96%. The filling gas was iso-octane and was maintained at a pressure of 3 torr. This detector is capable of better than 0.4 ns timing resolution and 1.6 mm position resolution, corresponding to one part in 2000 momentum resolution.

In order to measure the Z, KE, θ, and ϕ (nuclear charge, kinetic energy, emission angles, respectively) of each ion, a set of detectors was placed at the Final Achromatic Image of the mass separator. Two parallel plate avalanche counters (PPACs) measured the position of each ion with 1 mm resolution and were separated by 420 mm. The measured positions were used to calculate θ and ϕ. A 0.0001 cm thick Bicron BC404 scintillating foil was mounted on a plastic light guide and optically coupled to an RCA RC232 photomultiplier tube (PMT). The PMT signal from this detector was combined with the time information from the multistep detector at Image #1 to measure the time of flight of the ions over the 13.811 m flight path. With this pair of detectors, a time-of-flight resolution of about 0.6 ns was obtained for the reaction products. A four-element silicon detector telescope provided ΔE and total energy measurements for each ion. The silicon detectors, labeled ΔE1, ΔE2, ΔE3, and ΔE4, were 51.4, 51.5, 319, and 540 μm thick, respectively. Detectors ΔE1 and ΔE2 were totally depleted planar surface barrier silicon detectors with a thickness uniformity

of better than ±0.2 microns. Detectors ΔE3 and ΔE4 were totally depleted surface barrier silicon detectors. The ΔE3 detector suffered radiation damage during the experiment and was replaced part way through the experiment with a 500 μm partially-depleted detector. Each of the silicon detectors had an active area of 300 mm^2. All the silicon detectors were cooled to -20^0 C to reduce the thermal noise and thereby improve the signal-to-noise ratios. Nuclear magnetic resonance (NMR) probes in each of the dipole magnets were used to determine the magnetic fields.

A. Calibration and Isotope Identification

The detection system was calibrated by transporting various primary beam analogues directly through the A1200 spectrometer. These beams have very similar charge–to–mass ratios and are commonly used to calibrate detector systems [44]. Since the reaction products were highly stripped when exiting the target, an Al target was used to strip the calibration beams. These ions with known energies and masses were used to calibrate the Image #1 (horizontal) position measurement (X) versus the rigidity and the detector telescope.

The flight time was calibrated by setting all the magnets so that the beam traveled along the central trajectory of the A1200 magnetic spectrometer, where the path length could be determined most accurately. Since the beam energy is known and the path length is fixed, the flight time can be calculated, and thus determine the time offset resulting from the cable delays. The slope of the time calibration was determined by using a precision time calibrator. The common technique to prevent unnecessary starts of the TAC was used in which the "start" signal for the TAC came from the focal plane detector.

The calibration of the silicon detectors was performed in two stages. The initial energy loss calibration relied on ionizing trace impurities in the ECR source that were extracted and accelerated in the K1200 cyclotron. Low beam intensities (100-1000 particles/s) were required since these calibration beams impinged directly on the detector telescope. Beams used were $^{65}Cu^{14+}$, $^{83}Kr^{18+}$, $^{97}Mo^{21+}$, $^{130}Xe^{29+}$, and $^{134}Xe^{29+}$ at 50 MeV/nucleon; $^{84}Kr^{17+}$

and $^{94}Mo^{19+}$ at 40 MeV/nucleon; and $^{86}Kr^{14+}$ and $^{92}Mo^{15+}$ at 26 MeV/nucleon. The energy lost in each detector by each calibration beam was calculated using standard energy-loss tables [45]. These calculated energy losses in each detector were plotted versus the measured peak position. This first stage energy loss calibration proved adequate to provide an initial Z calculation using the equation

$$Z = a \cdot (\Delta E * E_{total})^{\frac{1}{3}} + b \cdot \Delta E \tag{1}$$

The Z of each ion was calculated using the ΔE values from both ΔE1 and ΔE2. This procedure provided a redundant Z determination for each ion, and the two calculations were averaged to improve the Z resolution.

The first stage isotope identification and an improved energy loss calibration were obtained by plotting the extracted Z value versus the measured time of flight (see Figure 2). This two-dimensional scatter plot shows the resolved elements as horizontal ridges. Since the A1200 accepts a small momentum range (only $\pm$1.5% of the central momentum), the individual isotopes of a given element are separated in time and appear as bumps along each ridge. There is one complication in this simple picture. An ion with a given mass to charge ratio, A/q, is only slightly separated in time-of-flight from ions with the same Z but having $(A+2)/(q+1)$ or $(A-2)/(q-1)$. This separation is about 0.4 ns, which is less than the experimental timing resolution of 0.6 ns. Therefore, it was not possible to separate isotopes with very similar A/q by gating on this spectrum only. Elastically scattered beam particles were also present in this spectrum, indicating the position of the ^{129}Xe ions. Furthermore, peaks in the time dimension for each Z value were visible and well resolved. For the 40 and 50 MeV/nucleon runs at low rigidity, a vertical line of spots was produced at small time of flight due to a sequence of ions with (A/q)=2. With this characteristic reference line, the peaks for the lower Z values ($20 \leq Z \leq 30$) were easily assigned to a given isotope, as these ions should be fully stripped at these high beam energies.

For the second stage of the calibration, eighteen isotopes from various regions of this two-dimensional spectrum were chosen as calibration isotopes. Each selected ion was also

required to travel along the central ray of the spectrometer by a software gate on the Image #1 position. By requiring this condition, the energy of each ion could be easily calculated and the selected ion separated from other ions with similar A/q values. This software condition restricted ions at the Image #1 X position to be within 3 mm of the central bend radius. Energy spectra from each silicon detector for each selected isotope were obtained. The error in E_{total} calibration was typically less that .5%.

The second stage Z calibration was obtained by using the improved energy loss calibrations. The final experimental Z resolution for the 40 MeV/nucleon data is shown in Figure 3 ($\sigma(Z) = .36$ esu). This calibration procedure was repeated for each beam energy and similar KE, Z, A, and Q resolutions were obtained in each case.

The mass of each ion was calculated from its measured total energy and time-of-flight data using the equation

$$A = \frac{E_{total}}{931.496(\gamma - 1)} \tag{2}$$

where A is in atomic mass units and E_{total} is in MeV. By substituting this equation into

$$B\rho = \frac{m\beta\gamma}{q} \tag{3}$$

where the usual relativistic parameters are

$$\beta = \frac{v}{c} \tag{4}$$

$$\gamma = \frac{1}{\sqrt{1 - \beta^2}} \tag{5}$$

where v is the ion velocity and c is the speed of light, and solving for q, one obtains

$$B\rho = 3.10711\beta\gamma\frac{A}{q} \tag{6}$$

$$q = \frac{3.10711}{931.496}\frac{E_{total}}{B\rho(\gamma - 1)}\beta\gamma \tag{7}$$

where q is in units of electronic charge and $B\rho$ is in Tesla-meters. A histogram of the calculated q is shown in Figure 3 and indicates the good resolution achieved ($\sigma(q)$=0.28

esu). Since q must be an integer and the mass resolution was limited by the error in the total kinetic energy measurement, the calculated q was rounded to the nearest integer and the mass was recalculated using an integer q in the equation

$$A = \frac{B\rho q}{3.10711\beta\gamma} \tag{8}$$

giving A in atomic mass units again. A typical mass spectrum is shown in Figure 3 and indicates the good mass resolution achieved ($\sigma(A) = 0.35$ amu).

B. Momentum Distribution Calculation

The momentum, p, of each particle was calculated using the equation:

$$p = 931.496\frac{B\rho q}{3.10711 \cdot A} \tag{9}$$

where the calculated A and q values are used. The momentum distributions of the reaction products are much wider than the 3% momentum acceptance of the A1200. To cover the entire momentum range, a number of runs were made using different magnetic field settings. Each run had central momenta differing by 2% from the neighboring runs. The momentum acceptance was not uniform at 100% across the full momentum range. It has been shown [46] that the momentum acceptance of the A1200 drops by 10% at 1% from the central ray and as much as 30% at 1.5% from the central ray. To correct for the limited acceptance, the momentum distribution for each run was multiplied by the reciprocal of the acceptance function.

Four PIN diodes were placed symmetrically around the target and were used to measure the beam current. The count rate of the PIN diodes was related to the beam current so that the absolute beam flux for each run was known. The momentum distributions from each run were normalized using the beam flux and then added together. Some gaps in the distributions were caused by the tremendous amounts of scattered beam at a few particular momenta. The edges of the measured momenta were located and each gap was

filled by interpolating between the edges. This final correction permitted the compilation of momentum distributions for all the ions with $Z > 39$.

The momentum distributions of interest are actually the distributions for each isotope as it exits the target rather than the distributions of each ion at the focal point. To produce this isotopic momentum distribution, all the momentum distributions for the charge states of each isotope must be summed. Since the ions have passed through the start detector, the charge state of the ion may have been changed at this point. Ion–optical calculations showed that, if the charge state of an ion changed in the start detector, the focus for that ion occurred at a different point at the final image of the spectrometer [47]. The focus of charge-changed ions was displaced horizontally from the original focal point of the spectrometer by about 4 cm for the case of q=50 and Δq=1. This displacement caused the charge-changed ions to miss the silicon detector stack and thus they were not observed. To account for this loss, it was assumed that ions passing through the start detector recreated their equilibrium charge state distribution. Charge state equilibrium was attained for 50 MeV/nucleon ^{129}Xe in carbon for all thicknesses greater than 1 mg/cm^2. This assumption was checked by measuring the charge state distribution for 1.0, 1.3, and 2.0 mg/cm^2 thick carbon foils. The measured charge state distribution did not change as a function of carbon foil thickness. Since the start detector is made of plastic foils and filled with iso-octane, carbon is a good approximation of its material composition. The areal thickness of the start detector was 1 mg/cm^2, and thus the assumption of the start detector recreating charge state equilibrium is reasonable. To create the final isotopic momentum distribution, the distributions for each charge state of an isotope were summed after the correction for charge change in the start detector had been applied. Figure 4 shows the momentum distribution for each charge state of ^{104}Sn after corrections and the final summed momentum distribution.

This process yields the momentum distribution for each isotope over the angular range of 0 to 24 mrad. Since the reaction products were distributed over a wider angular range, to extract the absolute yield of an isotope the effects of the limited angular acceptance must be removed. The angular spread of the ions was calculated assuming an incomplete

fusion reaction mechanism. (See Section IV.B.*1* for a description of the incomplete fusion calculation.) The width of the angular distribution results primarily from evaporation from the fused product. This width was only slightly changed by using a Boltzman–Nordheim–Vlasov model of the reaction mechanism. (See Section IV.B.*3* for a description of the Boltzman–Nordheim–Vlasov calculation.) Figure 5 shows the A1200 angular acceptance in the top frame. The calculated laboratory angular distributions for various Z-values are shown in the bottom frame. The fraction of the angular distribution that was contained within the angular acceptance of the A1200 was calculated. The yields for each isotope were then multiplied by the reciprocal of the acceptance fraction. This final correction allowed the compilation of the absolute production cross section for each isotope from each reaction. The error in the absolute yield of each isotope from the counting statistics is typically less than 10%. However, the beam current measurement did not work very well and a factor of four systematic error in the absolute beam flux is possible. This results from a poor normalization of the PIN diode count rate to the beam current.

III. EXPERIMENTAL RESULTS

A. Momentum Distributions

The momentum of each particle was calculated using the equation

$$p = 931.496\frac{B\rho q}{3.10711 \cdot A} = 931.496\beta\gamma c \tag{10}$$

where p is the momentum per nucleon in MeV/c/u and u is the atomic mass unit. The $\beta\gamma$ product was not calculated from the time-of-flight measurement but rather deduced from the Bρ calculated from the NMR reading and the bend radius measured at Image #1. This Bρ determination was used because it was more accurate than the time-of-flight measurement. Typical momentum distributions from the 50 MeV/nucleon ^{129}Xe + Al reactions are shown in Figure 6 for representative light, medium, and heavy isotopes of selected elements. The momentum distribution for each isotope of Sn and Mo are shown in Figure 7. The

fluctuations in the curves are due to low statistics. For a given element, the momentum distributions of the light mass isotopes peak near the momentum per nucleon of the beam, whereas the momentum distributions of the heavier isotopes peak at lower values. The momentum distribution of the heaviest isotope of the elements close to Z=40 extend almost down to the momentum per nucleon corresponding to complete fusion. These differences are most distinct in the data from the ^{129}Xe+Al reaction and are less apparent in the data from the Be and C targets due to the smaller range of momentum between the momentum per nucleon of the beam and that of the center of mass. The data from the two lower beam energies exhibit similar behavior. (Momentum distributions for all elements for the 50, 40, and 26 MeV/nucleon ^{129}Xe + Be, C, Al reactions are contained in [48].)

B. Isotopic Distributions

The absolute cross section for the production of each isotope was determined by integrating its momentum distribution. The measured isotopic cross sections for each of the nine target–beam energy combinations are shown in Figures 8, 9, 10, and 11 for isotopes with $Z > 39$. The overall dependence of the isotopic cross sections on bombarding energy and target mass is best seen in Figure 11. The yield for the lighter elements produced in the reaction of the 26 MeV/nucleon ^{129}Xe with the light targets is quite low (as also indicated in Figure 10), and the cross sections are more uncertain. The low counting statistics lead to the large fluctuations in the data between neighboring isotopes (e.g. a factor of 5 for Z=40 in the 26 MeV/nucleon ^{129}Xe + Be reaction).

A peak at A=129 is clearly visible in the Z=54 curve in Figures 8, 9, 10, and 11. This peak arises from (elastic) scattering of the incident beam. The yield of fragments with low Z values increases as the target mass increases at a given beam energy (see Figure 11). The yield of these light fragments also increases as the beam energy increases. Both of these trends parallel an increase in center-of-mass energy, as shown in Table I. Generally, events with high excitation energies emit a larger number of particles while de-exciting than

do events with low excitation energies and this leads to increased yields of lower Z value elements.

To better see the dependence of the isotopic yields on bombarding energy the isotopic cross sections in the A versus Z plane are shown in Figure 12. The stable isotopes are marked with filled squares in these figures. The stair-stepping line indicates the proton-rich limit of the known nuclei. These figures clearly show that the isotopes produced in these reactions all have lower A/Z ratios than the stable nuclei indicating substantial neutron evaporation. Also visible in these figures is the increasing yield of low Z value fragments with increasing center-of-mass energy.

In Figure 13, the average mass of each element is shown for the 50 MeV/nucleon ^{129}Xe + Be, C, and Al reactions. In the lower portion of this figure, the width of the mass distribution for each element is shown. This figure shows that the average mass and the width of the mass distribution for each element are independent of the target. A similar target independence is also seen for the other two beam energies.

Previous γ-ray spectroscopy studies of heavy residues have extracted the average Z value for each isobar. The line following the average Z value for each isobar is comparable to the ridge in the isotopic cross section distribution from the current data set. Similar energy ^{12}C + $^{107-109}$Ag reactions have been studied using γ-ray spectroscopy [28]. This allows a comparison between the ^{12}C + Ag data and the present ^{129}Xe + C data. In Figure 14, the average Z value for each isobar from the reaction of ^{12}C + Ag [28] (diamonds) is compared with the isotopic cross section distributions from the ^{129}Xe + C (contours) reactions measured with the A1200 spectrometer. Although the ranges of elements measured only partially overlap, it is clear that the isotopes produced in the ^{129}Xe-induced reactions are significantly more proton-rich than those produced in the ^{12}C + Ag reaction. The ^{12}C + Ag reaction products become less proton-rich with increasing bombarding energy, whereas the yields from the ^{129}Xe + C data show no such dependence on the bombarding energy. These differences may be the result of the inability of the γ-ray spectroscopy to measure very short-lived nuclei; however, it is difficult to prove that this is the cause of the differences.

A previous study measured part of the isotopic yields from the 70 MeV/nucleon ^{92}Mo + ^{58}Ni reaction [49]. These yields are shown as histograms in Figure 15. Since this system was studied using a magnetic spectrometer, it is not subject to the experimental restrictions of the γ-ray spectroscopy. However, these data were collected over a narrow range of magnetic rigidities and may be biased towards those nuclei with $A = 2Z$. For comparison, the isotopic cross sections for the same elements from the 50 MeV/nucleon ^{129}Xe+Al reaction are shown as continuous curves. The centroid values of these distributions are similar, but the isotopes produced in the ^{92}Mo + ^{58}Ni reaction are slightly more proton-rich, as might be expected given the more proton-rich target and projectile combination.

C. Elemental and Isobaric Yields

Previous studies of similar systems have measured the elemental and isobaric cross sections. In this study, the isotopic cross sections can be obtained by integrating the isotope's momentum distribution. The isotopic cross sections for all of the isotopes of each element can be summed to produce the elemental cross sections. These elemental cross sections are shown by the diamonds in Figure 16. The elemental cross section distributions become wider at higher beam energies and for heavier target nuclei. This effect was seen in the isotopic yields for isotopes with low Z values. Previous measurements of the elemental cross sections from similar systems are plotted as pluses [36–38]. Note that the cross sections measured in the present work cover a range of elements not measured in the complex fragment studies. Although the elements that have been previously measured do not significantly overlap the current data, the two data sets seem to be consistent. Notice that a large fraction of the total reaction cross section was missed in the previous studies of complex fragments.

The isobaric cross sections are the most accurately determined yields from γ-ray spectroscopy studies because the calculation of these yields requires the smallest number of assumptions. The isotopic cross sections for all the isotopes of each isobar from the present study were summed to produce isobaric cross sections. These isobaric cross sections are

shown by the continuous curves in Figure 17. Also shown in Figure 17 are the isobaric cross sections (measured using γ-ray spectroscopy) from similar reactions measured by Lleres [50]. These data sets are shown as pluses and times symbols with the ^{129}Xe-induced reaction from the present work that most closely approximates the ^{124}Sn reaction. Since the reactions presented for comparison have similar target and projectile masses and bombarding energies and the center-of-mass energy is large in all cases, the nuclear structure effects for a particular beam and target combination should be minimized and the resulting isobaric cross sections should be and generally are similar. The ^{129}Xe + Al data compares better with the ^{20}Ne + ^{124}Sn results than with the ^{40}Ar + ^{124}Sn results. This is reasonable because the excitation energy of the compound nucleus rapidly increases with the mass–symmetry of the entrance channel. There remains a deficit in the isobaric yields from the γ-ray spectroscopy studies. Such a deficit maybe due to the difficulty of measuring nuclei near stability with the γ-ray technique.

Figures 16 and 17 show that the shapes of the cross section distributions for the present and previous studies are similar. This agreement is consistent within the experimental uncertainties associated with the different measurements. The data from the present study at 26 MeV/nucleon appears to be low in comparison to the previous work. This may be due to the complications of measuring the many atomic charge states present at the lowest beam energy. The overall agreement also gives confidence in proceeding to compare the absolute cross sections with the results of model calculations.

D. Z versus Velocity Distributions

Previous studies of complex fragment emission have presented distributions of Z_{total} versus $\mathbf{v}_{source}$ [21,29,38,36]. The source velocity, $\mathbf{v}_{source}$, is defined as

$$\mathbf{v}_{source} = \frac{\Sigma m_i \mathbf{v}_i}{\Sigma m_i} \tag{11}$$

where m_i and $\mathbf{v}_i$ are the mass and velocity, respectively, of the i-th detected complex fragment. These distributions were used to determine the velocity of the source of the complex

fragments. Similar information about the source of the heavy residues in the present work can be extracted by integrating the isotopic momentum distributions over A and converting momentum to velocity to produce comparable Z value versus velocity distributions. These distributions for all the reaction systems in the present work are shown in Figure 18. For comparison, complimentary complex fragment data are also shown. (The ^{139}La data has been shifted down by 3 units of Z to account for the difference in Z values between $^{139}_{57}$La and $^{129}_{54}$Xe.) The data at higher velocity in each frame of Figure 18 are from this work; the data at lower velocities, noted with "CF", are taken from the referenced complex fragment studies. Figure 18 clearly shows the complimentary nature of the present measurements to the studies of the complex fragments. The cross section contours mesh together well and indicate that a complete measurement of the reaction requires both techniques.

E. Summary of the Experimental Results

The data for the ^{129}Xe–induced reactions was presented and compared to similar data from previous measurements of similar reaction systems. In general, the new data is consistent with the previous data. The new information available in the present data includes the elemental cross sections for the high Z value elements ($Z \geq 39$), the yield of fragments at velocities near that of the beam, the isotopic cross sections for part of the elemental yield range ($Z \geq 39$), and the momentum distributions for the high Z value isotopes. By combining the present data with the previous data, elemental cross sections from Z=6 to Z=57 are available. The present experiment measured fragments with a range of velocities not seen in the complex fragment data.

IV. DISCUSSION OF DATA AND MODELS

Previous studies of the 14 to 50 MeV/nucleon ^{129}Xe + C and ^{139}La + C reactions have demonstrated that one source of complex fragments is the statistical decay of a compound

nucleus [17,37,37,38]. At low bombarding energies ($E/A < 25$ MeV), the compound nucleus is formed in complete fusion reactions. At higher bombarding energies ($E/A > 30$ MeV), incomplete fusion of the reaction partners forms a range of compound nuclei with different masses and excitation energies. The complex fragments from these reactions have isotropic center-of-mass angular distributions ($d\sigma/d\theta$) and center-of-mass emission velocities dominated by the Coulomb repulsion of the two decay partners. These two features indicate a relaxed and long-lived source (source lifetime $\gg$ rotational period). In addition, the source velocities (v_{source}) extracted from analysis of both single-particle inclusive data and coincidence data are consistent and fall within the range expected from the complete or incomplete fusion reaction mechanism. The v_{source} value is used to calculate the amount of transferred mass and the excitation energy, which in turn is used in a statistical de-excitation model to calculate the complex fragment production cross sections. The agreement between the experimental and predicted cross sections, angular distributions, and emission velocities shows the validity of the compound nucleus source assumption.

As the present experiment is able to detect all the heavy residues produced in these reactions, several new questions can be addressed:

1. From the experimental standpoint, do the heavy residues come from the same source as the complex fragments, or do they result from a different source?

2. From the theoretical standpoint, if the heavy residues have the same source as the complex fragments, can the models that successfully predicted the complex fragment production also predict the heavy residue production?

3. From the practical standpoint, what is the source of the extremely proton-rich nuclei observed recently? The proton-rich nuclei are ^{61}Ga, ^{62,63}Ge, ^{65}As, ^{66}Se, ^{69}Br, and ^{75}Sr from 65 MeV/nucleon ^{78}Kr + ^{58}Ni [41,51]; ^{78}Y, ^{82}Nb, ^{84,85}Mo, ^{86}Tc, and ^{89,90}Ru from 70 MeV/nucleon ^{92}Mo + ^{58}Ni [49]; ^{94,95}Ag from 70 MeV/nucleon ^{106}Cd + ^{58}Ni [52]; and ^{101,102}Sn from 58 MeV/nucleon ^{112}Sn + Ni [53]. These nuclei are important

to nuclear structure studies, and understanding their production mechanism would facilitate these studies.

To address these questions, the data are first qualitatively examined for signatures of the reaction mechanism (Section IV.A). Then, two models of the reaction mechanism are compared to the previous and present data sets to test how well these models quantitatively describe the data (Section IV.B). It will be shown that the isotopic cross sections and momentum distributions from the present study do, in fact, provide a new, previously unavailable test of reaction model predictions.

A. The Velocity as a Function of Z

In previous complex fragment studies, two-dimensional distributions of the cross section as a function of Z_{total} and v_{source} have been created, where Z_{total} and v_{source} are the total charge and the center-of-mass velocity of the detected complex fragments, respectively. There are typically one to five heavy fragments and many light particles in the exit channel of the studied reactions. The heavy fragments move relative to one another with a well-defined velocity determined mainly by the Coulomb repulsion energy between the fragments. The evaporation of light particles either preceding or following the heavy fragment emission acts increase the width of the v_{source} distribution. The kinematic skeleton of the source breakup is not altered by isotropic ($d\sigma/d\Omega$) evaporation. Thus, the experimentally accessible v_{source} value corresponds closely to the velocity of the emitting source. For complete fusion reactions, v_{source} is equal to the velocity of the center of mass (v_{cm}). In incomplete fusion reactions, only a fraction of the lighter nucleus fuses with the heavier nucleus. When the projectile is larger than the target, v_{source} is larger than v_{cm} but smaller than the velocity of the beam (v_{beam}). The v_{source} is near the v_{beam} for small mass transfers, and the v_{source} is near the v_{cm} for nearly complete mass transfers. Therefore, an accurate determination of v_{source} should allow one to infer the amount of mass transferred.

For the 18 MeV/nucleon ^{139}La+C and the 26 and 31 MeV/nucleon ^{129}Xe + C reactions

[17,21,38], a single peak is observed in the reconstructed v_{source} distribution. Its centroid is at v_{cm}. The isotropic center-of-mass angular distributions ($d\sigma/d\theta$), the Coulomb–repulsion–dominated emission velocities, and the elemental cross sections of the complex fragments are all consistent with these reactions being dominated by complete fusion processes that result in compound nuclei. For the Xe(La) + Al and higher energy Xe(La) + C reactions (18 MeV/nucleon ^{139}La + Al, 26 and 31 MeV/nucleon ^{129}Xe + Al, and 35 to 55 MeV/nucleon ^{139}La+ C, Al reactions [17,36–38,54]), again a single peak in the v_{source} distribution was observed, but the centroid value was between the values of v_{cm} and v_{beam}, consistent with an incomplete fusion reaction mechanism. For the Xe(La) + Ti, Ni, and Cu reactions (18 MeV/nucleon ^{139}La + Ti and Ni reactions and 26 and 31 MeV/nucleon ^{129}Xe + Ti and Cu [21,38]), a range of values for v_{source} was observed, suggesting a broad range of mass transfers resulting from incomplete fusion reactions.

In the studies mentioned above, complex fragments emitted from compound nuclei have been detected. However, these compound nuclei can also de-excite by emitting only light particles ($Z \leq 2$), leaving a single cold heavy residue. For low excitation energies, complex fragment emission is an unlikely de-excitation process; thus, experiments that measure only the complex fragment production cross sections have missed a large portion of the primary yield. The Z_{total} versus v_{source} distribution for complex fragment coincidence events should have the same correlations as the Z value versus velocity distributions for the heavy residues, since both evaporation residues and complex fragments can result from the same nuclear reaction mechanism. The experimentally determined Z value versus velocity distributions for the heavy residues are shown in Figure 18. The distributions of Z_{total} versus the v_{source} derived from the complex fragment coincidence events from similar reactions are also shown in Figure 18.

The shapes of the Z value versus velocity distributions qualitatively support the incomplete fusion reaction mechanism, as illustrated in Figure 19. The solid line represents the range of values of velocity and Z value for the primary products that result from the incomplete fusion reactions of a large projectile nucleus with a small target nucleus. The

excitation energy of these products increases systematically with decreasing velocity. The amount of excitation energy depends directly on the amount of mass transferred and on the bombarding energy. Tables II and III show the excitation energies for ^{6}Li and ^{12}C transfers at 26, 40, and 50 MeV/nucleon in the ^{129}Xe + Al reaction. The excitation energies are calculated using the incomplete fusion model described in Section IV.B.*1*. This excitation energy is lost primarily through evaporation. Statistical decay calculations show that, on average, a charge is evaporated for approximately every 50 MeV of excitation energy. Using this result, the average evaporation residue Z value can be calculated. The result of this calculation is also shown in Tables II and III. Notice that the same mass transfer at a higher bombarding energy results in higher excitation energy and a lower average residue Z value. In Figure 19, the dotted line qualitatively indicates the nuclear charge of the incomplete fusion residues after evaporation for a low bombarding energy. As the bombarding energy increases, the excitation energy produced in the reaction increases and the locus of the final fragments rotates clockwise because of increased charged–particle evaporation. The two dashed lines schematically indicate the nuclear charge after evaporation for two higher bombarding energies.

The heavy residue data from the 26 MeV/nucleon reactions have almost no variation in the centroid value of the Z distribution as a function of velocity. This indicates that there is a balance between the charge gained in the incomplete fusion process and the charge lost via evaporation during the de-excitation. In the higher energy reactions, the centroid value of the Z distribution decreases as the velocity decreases, indicating that more charge is lost by evaporation than is gained in the incomplete fusion process.

The incomplete fusion reaction mechanism also qualitatively explains the range of velocities seen for each data set in Figure 18. Within a given bombarding energy, small mass transfers result in primary fragments with high velocities, small amounts of excitation energy, and low angular momenta. The low excitation energy and angular momentum give the resulting compound nucleus a low complex fragment emission probability, and thus a large probability of producing an evaporation residue. In contrast, large mass transfers result

in primary fragments with lower velocities, higher excitation energies, and higher angular momenta. The higher excitation energy and angular momentum give a higher complex fragment emission probability and a lower probability of producing an evaporation residue.

In the present experiment, when the incomplete fusion product emits a complex fragment, the resulting decay products are rarely detected, as the recoiling nuclei are usually outside the spectrometer acceptance. Thus, the depletion of heavy residues at low velocities (i.e., near v_{cm}) in the ^{129}Xe+Al reactions results from high excitation energies in the primary fragments. The primary fragments' concomitant high probability of emitting a complex fragment results in their low probability of detection in the current experiment. In contrast, the high probability of emitting a complex fragment gives large mass transfer, low velocity events a higher detection probability in complex fragment experiments. This is why the complex fragment data in Figure 18 are near v_{cm} for each reaction. Thus, the present Z value versus velocity distributions for the heavy residues fit nicely with the Z_{total} versus v_{source} distributions for the complex fragments (i.e. detecting the heavy residues is a good way to measure the cross section of small mass transfer events and detecting the complex fragments is a good way to measure the cross section of large mass transfer events). The combination of these data sets gives a complete picture of the reaction mechanism that can be understood within the framework of the incomplete fusion reaction mechanism. The qualitative agreement between the model and the data suggests that this reaction mechanism deserves further detailed investigation.

B. Model Calculations

In this section, the predictions from two models are discussed and compared with the data. These models are the incomplete fusion (ICF) model and the Boltzman–Nordheim–Vlasov (BNV) model. It has been shown that an incomplete fusion reaction mechanism qualitatively explains the data (see Section IV.A) and both the ICF and BNV models can produce incomplete fusion–like reactions (i.e. the larger nucleus picks up mass from the

smaller nucleus). The BNV model is able to simulate pre-equilibrium emission of nucleons, whereas the ICF model can not. Pre-equilibrium emission can have significant effects at the bombarding energies used in the present work and thus the BNV model is a useful companion to the ICF model. Neither of these models is capable of calculating the de-excitation of the excited fragments. To remedy this problem, both models are coupled to a statistical decay model which simulates the de-excitation process.

Both models have been used previously to predict the data from similar reactions. The ICF model [37] has been successful in explaining many features of complex fragment emission from the 26 MeV/nucleon ^{129}Xe + C, Al, Ti, and Cu reactions [38]. The BNV model has been successful in explaining certain aspects of the complex fragment data from the 55 MeV/nucleon ^{139}La + Al [55,56] and 50 MeV/nucleon ^{129}Xe + C, Al, V, Cu, Y, and Au reactions [57].

1. Incomplete Fusion Calculation

Predicting the final residue products from the incomplete fusion reaction involves two stages. The first stage is the incomplete fusion process. The second stage is the statistical decay of the excited fragments produced in the incomplete fusion process. (For clarity during the following discussion, "ICF model" refers only to the model of the first stage, whereas "ICF calculation" refers to the result of using the primary fragments from the ICF model as input to the statistical decay calculation.)

In the first stage of the calculation, a geometrical incomplete fusion model [37] is used to describe the dynamics of the reaction in which two sharp spheres represent the colliding nuclei. The energetics of fragment formation is assumed to be dominated by the increase in the surface area of the fragments. Since the surface area created by breaking the smaller nucleus into parts is less than the area created by breaking the larger nucleus into parts, it takes less energy to break the smaller nucleus. To account for this, the model forces the overlapping nuclear matter to be sheared from the smaller target nucleus and fuses it

onto the the larger projectile nucleus to produce a compound nucleus plus a cold spectator. The model generates values for the Z,A, excitation energy, final spin J, and the laboratory velocity of each of the reaction partners. The excitation energy is calculated from the energetics of the surface creation and from the mass transfer. J is calculated from the relative motion of the centers of mass of the projectile and the lump of mass transferred from the target.

In the second stage of the calculation, the large excited primary fragment formed in the incomplete fusion process is assumed to de-excite statistically. The statistical decay of each fragment is simulated by using the Monte Carlo computer code GEMINI [17], in which all possible binary decays of the compound nucleus, from light particle emission to symmetric division, are considered. After each binary division, further decay of the resulting excited fragments is followed until all the available excitation energy is exhausted. Following the emission of a heavy fragment, the remaining excitation energy is divided under the assumption of equal temperatures in the two fragments. To calculate the spin of each fragment, the angular momentum is partitioned in the sticking limit. Thermal fluctuations in both the division of the excitation energy and the partition of angular momentum are incorporated. The decay widths for the evaporation of light particles ($Z \leq 2$) are calculated using the Hauser-Feshbach formalism [58]. The decay widths for the emission of heavy fragments ($Z \geq 3$) are calculated in GEMINI by using the transition state formalism of Moretto [59]. Details of these calculations are described in [17].

An ICF calculation was carried out for each reaction studied in the present work. All the parameters of the statistical decay model were set to standard values. The only adjustable parameter in the ICF model was the radius parameter (r_0), used to calculate the size of the sharp spheres.

$$R_{sharpsphere} = r_0 A^{\frac{1}{3}} \tag{12}$$

In this model, sharp-surfaced spheres were used to represent the nuclei. In reality, the nuclear surface is diffuse, so r_0 was assumed to be slightly adjustable.

It has been shown that the ICF calculations are sensitive to the value chosen for the radius parameter [38]. Hanold et al. used r_0 as a fitting parameter in this ICF calculation to reproduce the complex fragment data from the 26 MeV/nucleon ^{129}Xe + C, Al, Ti, and Cu reactions. The best agreement with the cross sections and the Z_{total} versus v_{source} distributions was obtained with a value of r_0=1.10 fm. In the present study, changing the radius parameter had no effect on the predicted average mass for each element. (The predicted average mass for each element is determined by the statistical decay calculation. See Section IV.B.*2*.) The predicted elemental cross sections, however, were sensitive to r_0, as the cross section for production of the heavy residues increased 20% and the cross section in the $10 \leq Z \leq 30$ region increased 50% when r_0 was increased from 1.10 fm to 1.25 fm. The increased cross section results from the increased range of impact parameters that led to collisions and a greater fraction of these collisions led to primary products with high excitation energy when r_0 was 1.25 fm. The high excitation energy gives a higher complex fragment emission probability and thus leads to the larger increase in the complex fragment cross sections. A radius parameter of 1.10 fm was found to give the best agreement with the data from the previous study, and it also gave good agreement with the present data set.

The results from the ICF calculations can be compared to the cross section data in Figures 16, 20, 12 and the momentum distributions in Figures 6 and 7. (Figure 16 shows the elemental cross sections from the ICF calculation as dotted curves.) Possible systematic experimental errors make the absolute cross sections uncertain by up to a factor of four. (The error in the magnitude of the yields primarily results from a poor measurement of the integrated beam current.) The magnitude of the cross sections from the ICF calculation is somewhat variable, since r_0 was taken to be adjustable. Therefore, the shape of the predicted elemental cross sections is a more sensitive test of the calculation than the magnitude. For the heavy residues, the cross section distributions predicted by the ICF calculation generally have the same shape as the experimental cross section distributions, but the predicted cross sections are larger in magnitude. The ICF predictions for the ^{129}Xe + C data agree with the complex fragment data at 26 and 40 MeV/nucleon but overpredict the complex fragment

yields at 50 MeV/nucleon. The ICF calculation for the ^{129}Xe + Al reaction only agrees with the complex fragment cross sections at 26 MeV/nucleon. The calculation for the 40 and 50 MeV/nucleon ^{129}Xe + Al reactions predicts complex fragment yields within an order of magnitude of the data, but the shape of the distribution is incorrect. Overall, the ICF calculation reproduces all the cross sections except for the complex fragment cross sections from the 40 and 50 MeV/nucleon ^{139}La + Al reactions.

The measured distributions of cross sections for fragments with $Z > 39$ as a function of Z value and velocity are shown in the first, third, and fifth rows in Figure 20. The second, fourth, and sixth rows show the predictions of the incomplete fusion calculation. Notice that the shape of the velocity distribution is closely predicted by the calculation. The ICF calculation also predicts the centroid value of the Z distribution correctly for all the targets and beam energies in this study. The width of the Z distribution for the 26 MeV/nucleon reactions is well reproduced, but the predicted width is too small by almost a factor of 2 for the 40 and 50 MeV/nucleon reactions.

The cross sections as a function of Z value and velocity are consistent with the incomplete fusion reaction mechanism, but the isotopically resolved momentum distributions provide a more detailed test of the model predictions. The momentum distribution for each isotope was extracted from the data, and the results are shown in Figures 6 and 7. The shape of the momentum distribution changes slowly with the mass of a given element (see Figure 7); therefore, only the momentum distributions for a representative light, average, and heavy isotope of each element are presented in Figure 6. The experimental momentum distributions can be compared to the predictions from the ICF calculations. The calculated momentum distributions are shown as dashed curves on Figure 6. Note that the model predicts the very proton-rich isotopes to have less than 50 nanobarn production cross section in these reactions. This is why there are no predictions shown with the momentum distributions for the proton-rich isotopes. The shape and width of the calculation's distributions are close to the shape and width of the experimental distributions, but the predicted centroid values of the momentum distributions for the heavy isotopes are too large.

Figure 21 shows the isotopic cross section distributions from the ICF calculation and from the experimental data. (Figure 16 shows that the predicted elemental cross sections from the ICF calculation are too large. This implies that the total of the predicted isotopic cross sections for each element is also too high. The magnitude of the predicted isotopic cross sections shown in Figure 21 is scaled to match the maximum heights of the experimental cross section distributions. This was done to allow easy comparison of the centroid values and widths of the predicted and experimental distributions.) The predicted average isotope of a given element has, typically, two more neutrons than the experimentally determined average isotope of that element. (Alternatively, Figure 21 could be made to join all the isotopes of each isobar rather than all the isotopes of each element. It would then appear that the calculation's average atomic number for each isobar is one atomic number less than the experimental average atomic number for each isobar.) Furthermore, the predicted width of the mass distribution of each element is smaller than the corresponding experimental width. Figure 12 shows as contours the isotopic cross sections for each reaction studied here. The predicted average mass for each element is shown as a solid line on these figures. The ridge in each isotopic cross section distribution is comparable to the solid line. The overprediction of the average mass of each element by 2 amu is seen for each system. Possible solutions of this disagreement are discussed in Section IV.B.*2*.

Overall, the ICF calculation gives an acceptable prediction of the results from this experiment. The shapes of the predicted elemental cross section distributions are correct for the heavy residues, and the predicted magnitudes of the cross sections are larger but are within the experimental uncertainty. The shapes of the cross section distributions as a function of Z value and velocity are closely predicted by the calculation. The calculation reproduces the shape and width of the momentum distribution for most isotopes well. The shapes of the calculated elemental cross sections for the complex fragments are correct for all the ^{129}Xe(^{139}La) + C reactions and for the 26 MeV/nucleon ^{129}Xe+Al reaction. The observed independence of the average mass for each element from the entrance channel (see Figure 13) is predicted by the ICF calculation. The average mass of each element, the width of

the mass distribution of each element, and the width of the Z distribution as a function of velocity are not well reproduced, however. The causes of these differences are examined further in the next section.

2. GEMINI AND THE ISOTOPE PREDICTIONS

The overprediction of the experimental average mass of each element and the underprediction of the widths of the final fragment distributions are the significant failings of the ICF calculation. Since changing the radius parameter (r_0) of the ICF model had no effect on these predictions, the statistical decay calculation was examined to determine whether it was the cause of these differences.

The A/Z ratio of the final fragments resulting from statistical decay is decoupled from the A/Z ratio of the primary fragment for sufficiently high excitation energies. Charity et al. [17] claimed that this decoupling occurs if the excitation energy is above 1 MeV/nucleon. In the present study, this excitation energy is easily reached for even small mass transfers. For the ICF model at 26 MeV/nucleon, this means transferring merely 4 nucleons, whereas at 50 MeV/nucleon, only 2 nucleons need be transferred.

To demonstrate the decoupling of the initial and final A/Z ratios at high excitation energies, the average mass of each element was calculated for two different systems. One system was very proton rich (Z=67, A=149, E^*=580 MeV, and J_{max}=110$\hbar$), and the other system was very neutron rich (Z=67, A=166, E^*=580 MeV, and J_{max}=110$\hbar$). The calculation used a $2J+1$ weighting at each J and J ranged from $J = 0\ \hbar$ to J_{max}. For each element, the average residue masses from these two systems differ by less than one mass unit over most of the Z range. This is shown in Figure 22. A second, simpler statistical decay model that allowed only the emission of γ-rays and evaporation of neutrons, protons, and alpha particles was run to check GEMINI's predictions. The results from this code (LOTO [60]) are consistent with GEMINI's results. Thus, the step in the ICF + GEMINI calculation that determines the average mass for each element is the statistical decay calculation, since

the A/Z ratio of the final fragments from GEMINI is decoupled from the A/Z ratio of the initial fragments input into GEMINI.

The isotopes predicted by GEMINI are less proton rich than the isotopes observed in the present work. Increasing the excitation energy of the initial fragments does not make the predicted final fragments more proton rich. Instead, increasing the excitation energy causes more evaporation, and the average residue mass decreases. This may indicate that the value of the binding energy for the neutrons used in the calculations is too high relative to the emission barrier for protons in proton-rich nuclei. The neutron and proton binding energies are unknown for these nuclei, since the masses of many proton-rich nuclei seen in this work have not been measured. An extended liquid drop model [61] of the ground state nuclear mass is used by GEMINI to calculate the neutron and proton binding energies for proton-rich nuclei. This mass model has a root-mean-squared error of 0.863 MeV for the ground state mass of the known nuclei. Small changes in the barriers for particle emission from the proton-rich nuclei may improve the agreement between the calculation and the data. For example, reducing the neutron binding energy of the proton-rich nuclei by 0.3 MeV reduces the average mass of each element by 1 amu. This change in the masses of the proton-rich nuclei is within the mass model's uncertainty, and thus the predicted average mass for each element can be brought into agreement with the experimental value.

In addition, there are other input parameters in the statistical decay calculation whose values are not well known. For example, the level density parameter (a) and the asymmetry parameter of the mass model are not well known. Small adjustments of these parameters may improve the agreement between the calculation and the data.

To investigate the effect of the level density parameter on the widths of the final fragment distributions, a was varied in the GEMINI calculations from $a = A/7$ to $a = A/10$. For $a = A/7$, the predicted average mass for each element decreased slightly ($< A_{a=\frac{A}{8.5}} > - < A_{a=\frac{A}{7}} >$=0.5) and the width of the isotopic cross section distribution decreased ($\sigma_{a=\frac{A}{7}}/\sigma_{a=\frac{A}{8.5}}$ = 0.75) relative to the predictions using $a = A/8.5$. With $a = A/10$, the predicted average

mass for each element increased slightly ($< A_{a=\frac{A}{8.5}} > - < A_{a=\frac{A}{10}} >$=–0.5) and the width increased ($\sigma_{a=\frac{A}{10}} / \sigma_{a=\frac{A}{8.5}} = 1.2$) relative to the predictions with $a = A/8.5$. When a decreased, the width of the distribution increased, but not enough to reproduce the data. Furthermore, the disagreement between the experimental and predicted average masses of each element became larger. These two opposite effects do not allow the simultaneous reproduction of both the average isotope for a given element and the width of the mass distribution for that element by solely varying a.

Adjusting the binding energy for the neutrons changes the proton richness of the final fragments. Decreasing a and decreasing the neutron binding energy have opposing effects on the proton richness of the final fragments. The neutron binding energy and a were used together as fitting parameters to make the ICF predictions and the experimental values for the centroids and the widths of the final fragment distributions consistent. Agreement between the model predictions and the experimental data was achieved by reducing the neutron barrier by 2 MeV and setting a equal to $A/15$. This large a variation of these parameters does not seem physically justifiable.

The mass asymmetry parameter can change the neutron and proton binding energies so that they do not vary as strongly with the A/Z ratio of the decaying nucleus. The final fragment distribution can be made broader by changing this parameter. Unfortunately, this change also destroys the mass model's ability to reproduce the known nuclear masses. This implies that varying the mass asymmetry parameter is not a good solution to the disagreement between the model predictions and the experimental data.

There are a few other options for improving the agreement between the calculations and the data. The A/Z ratio of a nucleus with low excitation energy ($E^* \leq 30$ MeV) is not changed very much by the de-excitation process. If the model of the collision stage produced a distribution of primary fragments that was similar to the experimental distribution, and these fragments had low excitation energies, then the subsequent de-excitation by GEMINI would not alter the primary distribution. The agreement between the prediction and the data would be improved. Excitation energies this low, however, are produced for only the

extremely peripheral collisions in the ICF model, and these collisions do not yield proton-rich primary fragments. This option is not available within the ICF model.

It was thought that the smaller predicted widths of the mass distribution for each element may result from the lack of fluctuations in the A/Z ratio of the transferred mass in the ICF model. Therefore, fluctuations in the A/Z ratio of the transferred mass were added to the ICF model. They had no effect on the final fragment distributions, however, since the final fragment A/Z ratio from GEMINI is decoupled from the initial fragment A/Z ratio.

It was thus found to be impossible to reproduce the final fragment distributions by using the ICF model coupled to GEMINI. This suggests that the most proton-rich fragments result from collisions that are not described within this model.

3. Boltzman–Nordheim–Vlasov Calculation

A second, somewhat different calculation was also compared to the data. A Boltzman–Nordheim–Vlasov (BNV) model [62,63] was used to simulate the dynamics of the reaction. Prediction of the detectable products from the BNV model involves two stages that are similar to the stages in the ICF calculation. The first stage is the dynamic stage of the collision. The second stage is the statistical decay of the excited fragments produced in the first stage. (For clarity during this discussion, "BNV model" refers only to the BNV model of the first stage, while "BNV calculation" refers to the result of coupling the BNV model to the statistical decay model.)

The dynamical stage of the collision was simulated by solving the BNV equation with the test particle approach in a "full ensemble" method (each nucleon being represented by 50 test particles). The self-consistent mean field potential and a nuclear potential approximated by a density dependent Skyrme–like interaction. The parameters of the latter potential were chosen to reproduce nuclear matter saturation properties and a compressibility coefficient of K=200 MeV. The free nucleon–nucleon cross section was used in the collision term with its energy and angular dependence. These are the same values used to reproduce ^{139}La +

Al data at the somewhat higher energy of 55 MeV/nucleon. The collision is followed as a function of time until the slope of the mean kinetic energy of the emitted nucleons versus time curve has changed. This sudden change of the slope is taken to indicate the transition from pre-equilibrium emission to evaporation from an equilibrated source. At the relaxation time (about 110 fm/c), where the slope of the emitted nucleons' mean energy versus time curve changes, a clustering procedure is used to calculate the Z, A, E^*, and J of each fragment. This procedure forms clusters from the test particles that satisfy the condition $\mid r_i - r_j \mid < D$, where r_i and r_j are the positions of the i-th and j-th test particles. D is set to the minimum value that allows the clustering procedure to reproduce the target and projectile masses at the start of the calculation (D = 1.5 fm). The angular momentum of the cluster is determined by summing the angular momentum of each particle:

$$J = \Sigma \, \mathbf{r}_i \times \mathbf{p}_i \tag{13}$$

in the cluster center of mass. The cluster excitation energy is

$$E^* = E_{kin} + E_{nmf} + E_{coul} - E_{gs} \tag{14}$$

where E_{kin} is the total kinetic energy, E_{nmf} is the nuclear mean field energy, E_{coul} is the Coulomb energy, and E_{gs} is the ground state total energy calculated from the static solution used as the initial condition for the BNV calculation. The Z, A, E^*, and J of the excited primary fragments at the relaxation time are then used as input values for a statistical decay code (in this case, GEMINI) to simulate the de-excitation process. This calculation is carried out for the entire range of impact parameters. The results for all the impact parameters are combined to give a prediction of the entire reaction.

In practice, the clustering procedure sometimes gave incorrect results at the relaxation time, because the primary fragments were not well separated. Fragments that were only slightly separated were frequently clustered together. To overcome this problem, the BNV calculation was extended to longer times (130 fm/c) where the clusters were clearly defined. The clusters' Z, A, E^*, and J were determined as a function of time. The functions for Z,

A, E^*, and J were extrapolated back to the relaxation time to obtain the Z, A, E^*, and J of the separated fragments at the relaxation time.

The BNV model produces one primary fragment for central collisions at 26 to 50 MeV/nucleon and two primary fragments for very peripheral collisions at 40 and 50 MeV/nucleon. Figure 23 shows a comparison of the calculated values for the mass, excitation energy, and velocity of the primary projectile-like fragments from both the BNV and the ICF models for the 50 MeV/nucleon ^{129}Xe + Al reaction. The crosses with the error bars represent the results and the uncertainties from the BNV model at each impact parameter. The uncertainty in the BNV result arises primarily from determining the relaxation time. The error bars represent variation of the relaxation time by ± 5 fm/c. The BNV model predicts smaller masses and excitation energies than the ICF model because pre-equilibrium emission is allowed in the former and not in the latter. The shapes of the velocity, mass, and excitation energy distributions for the primary projectile-like fragments, however, are very similar for both models (see Figure 23). This similarity is seen for all the 40 and 50 MeV/nucleon ^{129}Xe + Be, C, and Al reactions.

The BNV model predicted the formation of very elongated, rotating objects at 26 MeV/nucleon and large impact parameters. Even at times greater than 300 fm/c, the shape did not relax. Since the shape of the primary fragment had not relaxed by this time, the model result was not consistent with the assumption of equilibration within the model's usable time scale. In addition, the excitation energies for all impact parameters at 26 MeV/nucleon became negative between 160 fm/c and 220 fm/c after the start of the collision because of violation of the Pauli principle in the BNV model. The slope of the emitted nucleons' mean kinetic energy curve did not change until 120 fm/c to 130 fm/c. This required that the BNV model be run for longer times than it was for the 40 and 50 MeV/nucleon reactions. The longer time requirement, combined with the lower bombarding energy and increased overlap of the Fermi spheres, means that the Pauli-blocking violation is large. Therefore, the BNV calculations were not run for the 26 MeV/nucleon reactions.

Overall, the BNV model produced an incomplete fusion-like reaction (i.e. the projectile

nucleus picked up mass from the smaller target nucleus). The excited primary fragments from the BNV model were coupled to a statistical decay model to determine the final fragments. The results of these coupled model calculations are shown in Figure 24 for the 50 MeV/nucleon ^{129}Xe + Al reaction. Also shown in Figure 24 are the predictions from the ICF calculation and the experimental data. The predicted Z value versus velocity distributions and elemental cross sections from the BNV + GEMINI calculations are very similar to those from the ICF + GEMINI calculations. Both models give similar results for the average mass for each element, the width of the mass distribution for each element, and the momentum distributions for each isotope for all the 40 and 50 MeV/nucleon reactions studied. Since GEMINI was used to calculate the de-excitation stage, the BNV + GEMINI calculations also overestimate the average mass for each element and underestimate both the width of the Z distribution as a function of velocity and the width of the isotope distribution for each element. The cause of and solutions to these differences are discussed in detail in section IV.B.*2.*

In general, the differences between the ICF and BNV predictions are small; however, there is one significant difference. The ICF model predicts the production of a target remnant over a large range of impact parameters, whereas the BNV model predicts the production of a target remnant for only very peripheral reactions. For more central collisions ($b = 4$ fm), where the ICF model predicts a target remnant, the BNV model predicts that the mass not in the primary fragment is left in a few very small fragments ($Z \leq 2$) and many single nucleons. The present experiment is capable of detecting neither the target-like remnant nor a large number of single nucleons and thus can not distinguish between the ICF and the BNV model predictions.

The answers to the first two questions that were posed at the beginning of Section IX are now clear. It has been shown that heavy residues are produced in complete and incomplete fusion reactions. Models of these reaction mechanisms have predicted the complex fragment data well. These models also predict many aspects (e.g., the elemental cross sections, the cross sections as a function of Z value and velocity, and isotopically resolved momentum

distributions) of the heavy residue data reasonably well. The exception to this is that both models predict less than 50 nanobarn production cross section for the very proton-rich nuclei observed in this experiment. These models are able to reproduce the proton-rich nuclei only if currently accepted input parameters of the statistical decay calculation are strongly varied; however, these large variations are not physically justifiable. This suggests that the source of these extremely proton-rich nuclei must be a reaction that produces cold proton-rich nuclei. The details of this reaction mechanism are not understood within either model examined here.

V. CONCLUSIONS

The production cross sections of the residues with $Z > 39$, as a function of Z, A, and momentum, from the 26, 40, and 50 MeV/nucleon ^{129}Xe + Be, C, and Al reactions were measured by using a magnetic spectrometer. Combining the present and previous data, experimental cross sections spanning almost the entire range of Z values produced in these reactions have now been measured. The current data have been compared to those from previous works utilizing similar reactions. Although the elemental cross sections do not overlap previous measurements, they seem to be consistent with them. The isobaric cross sections generally agree with previous γ-ray spectroscopy measurements of the isobaric cross sections for similar systems.

Measurements of the isotopic cross sections by γ-ray spectroscopy have assumed a smoothly varying cross section distribution to extract the cross sections for the undetectable isotopes. The need for this premise results from the inability of γ-ray spectroscopy to detect short-lived isotopes ($t_{1/2} < 5$ minutes). The symmetry of the experimental isotopic cross sections (Figure 8) for each element and the smooth variation between elements confirm the validity this assumption.

The experimental Z value versus velocity distributions are consistent with the Z_{total} versus $\mathbf{v}_{source}$ distributions determined from complex fragment coincidence data. This study

provides a determination of the relative amounts of incomplete and complete fusion that is complementary to that implied in studies of complex fragments. Events with very low excitation energies are easily detected in the present work, since no fission-like decay is required. These distributions provide strong evidence for an incomplete fusion reaction mechanism.

Many features of the current data were reproduced by an incomplete fusion (ICF) model coupled to a statistical decay calculation. This calculation was able to reproduce the shapes of the heavy residue elemental cross sections and the Z value versus velocity distributions. The complex fragment emission velocities and cross sections from the 40 and 50 MeV/nucleon La + C reactions and the 26 MeV/nucleon Xe + C and Al reactions were well reproduced. The ICF calculation also predicted the independence from the entrance channel of the average mass for each element. The primary failures of this model are its overestimation of the average mass for each element and its underestimation of the widths of the Z distributions as a function of velocity and of the isotope distribution for each element. The momentum distributions provide a new test of the reaction model. The most proton-rich nuclei are predicted to have less than 50 nanobarn production cross section and thus have no predicted momentum distribution. The average mass isotope for each element typically has its momentum distribution well predicted by the model calculation. The heavier isotopes of each element are not as well predicted, as the predicted centroid values are too large.

The difference between the experimental and predicted average isotopes for each element can be eliminated by small, but systematic, variation of the input parameters for the statistical decay calculation. The width of the Z distribution as a function of velocity and the width of the isotope distribution for each element can not be reproduced with reasonable input parameters for the calculation. Overall, the incomplete fusion model coupled to a statistical decay model gives a fair representation of the data.

A Boltzman–Nordheim–Vlasov (BNV) model coupled to a statistical decay model yields essentially the same prediction as the ICF model for the heavy residue data from the 40 and 50 MeV/nucleon ^{129}Xe + Be, C, and Al reactions. Both models predict that the heavy

residues produced in this energy region result from incomplete fusion-like reactions (i.e. the projectile nucleus picked up mass from the smaller target nucleus). There is one significant difference between the predictions of the BNV and ICF models. The ICF model predicts the production of a target remnant over a large range of impact parameters, whereas the BNV model predicts the production of a target remnant for only very peripheral reactions. For more central collisions (b = 4 fm), where the ICF model predicts a target remnant, the BNV model predicts that the mass not in the primary fragment is left in a few very small fragments ($Z \leq 2$) and many single nucleons. The present experiment is capable of detecting neither the target-like remnant nor a large number of single nucleons and thus can not distinguish between the ICF and the BNV model predictions.

The very proton-rich nuclei detected in the present study are predicted to have less than 50 nanobarn production cross section by both models. The production mechanism for these very proton-rich nuclei, as well as the mechanism producing the extremely proton-rich nuclei observed recently, is not understood within the reaction mechanisms studied here. The models can predict the production of these proton-rich nuclei only if the statistical model input parameters are varied beyond the physically possible range. Therefore, these nuclei must be produced in a collision that makes the nuclei with almost no excitation energy. Any moderate amount of excitation energy would enable the nucleus to evaporate a proton and become less proton rich.

VI. ACKNOWLWEDGEMENTS

One author (K.H.) would like to thank the National Science Foundation for support under a graduate fellowship. This work was supported by the National Science Foundation and the Department of Energy under contracts PHY-92-14992 and DE-ACSO3-76SS00098, respectively.

REFERENCES

[1] E.K. Hyde, G.W. Butler, and A.M. Poskanzer, *Phys. Rev. C* **4**, 1759 (1971).

[2] A.M. Poskanzer, G.W. Butlet, and E.K. Hyde, *Phys. Rev. C***3**, 882 (1971).

[3] R.G. Korteling, C.R. Toren, and E.K. Hyde, *Phys. Rev.C* **7**, 1611 (1973).

[4] A.M. Zebelman, A.M. Poskanzer, J.D. Bowman, R.G. Sextro, and V.E. Viola, *Phys. Rev. C* **11**, 1280 (1975).

[5] J. Gosset, H.H. Gutbrod, W.G. Mayer, A.M. Poskanzer, A. Sandoval, R. Stock, and G.D. Westfall, *Phys. Rev. C* **16**, 629 (1977).

[6] W.G. Meyer, H.H. Gutbrod, C. Lukner, and A. Sandoval, *Phys. Rev. C* **22**, 179 (1980).

[7] C. Chitwood, D.J. Fields, C.K. Gelbke, W.G. Lynch, A.D. Panagiotou, M.B. Tsang, H. Utsunomiya, and W.A. Freidman, *Phys. Lett.* **B131**, 289 (1983).

[8] B.V. Jacak, G.D. Westfall, C.K. Gelbke, L.H. Harwood, W.G. Lynch, D.K. Scott, H. Stoker, M.B. Tsang, and T.J.M. Symons, *Phys. Rev. Lett.* **51**, 1846 (1983).

[9] L.G. Sobotka, M.L. Padgett, G.J. Wozniak, G. Guarino, A.J. Pacheco, L.G. Moretto, Y. Chan, R.G. Stokstad, I. Tserruya, and S. Wald, *Phys. Rev. Lett.* **51**, 2187 (1983).

[10] D.J. Fields, W.G. Lynch, C.B. Chitwood, C.K. Gelbke, M.B. Tsang, H. Utsunomiya, and J. Aichelin, *Phys. Rev. C* **30**, 1912 (1984).

[11] L.G. Sobotka, M.A. McMahan, R.J. McDonald, C. Signarbieux, G.J. Wozniak, M.L. Padgett, J.H. Gu, Z.H. Liu, Z.Q. Yao, and L.G. Moretto, *Phys. Rev. Lett.* **53**, 2004 (1984).

[12] M.A. McMahan, L.G. Moretto, M.L. Padgett, G.J. Wozniak, L.G. Sobotka, and M.G. Mustafa, *Phys. Rev. Lett.* **54**, 1995 (1985).

[13] F. Auger, B. Berthier, A. Cunsolo, A. Foti, W. Mittig, J.M. Pascaud, E. Plagnol, J.

Quebert, and J.P. Wieleczko, *Phys. Rev. C* **35**, 190 (1987).

[14] M. Fatyga et al., *Phys. Rev. Lett.* **58**, 2527 (1987).

[15] B. Borderie, M. Montoya, M.F. Rivet, D. Jouan, C. Cabot, H. Fuchs, D. Gardes, H. Gauvin, D. Jacquet, and F. Monnet, *Phys. Lett.* **B205**, 26 (1988).

[16] R. Bougault et al., *Nucl. Phys.* **A488**, 255c (1988).

[17] R.J. Charity et al., *Nucl. Phys.* **A483**, 371 (1988).

[18] R.J. Charity, D.R. Bowman, Z.H. Liu, R.J. McDonald, M.A. McMahan, G.J. Wozniak, L.G. Moretto, S. Bradley, W.L. Kehoe, and A.C. Mignerey, *Nucl. Phys.* **A476**, 516 (1988).

[19] L.G. Moretto and G.J. Wozniak, *Prog. Part. Nucl. Phys.* **21**, 401 (1988) and references therein.

[20] M.F. Rivet, B. Borderie, C. Gregoire, D. Jouan, and B. Remaud, *Phys. Lett.* **B215**, 55 (1988).

[21] N. Colonna et al., *Phys. Rev. Lett.* **62**, 1833 (1989).

[22] D.E. Fields et al., *Phys. Lett.* **B220**, 356 (1989).

[23] H.Y. Han, K.X. Jing, E. Plagnol, D.R. Bowman, R.J. Charity, L. Vinet, G.J. Wozniak, and L.G. Moretto, *Nucl. Phys.* **A492**, 138 (1989).

[24] R.J. Charity et al., *Nucl. Phys.* **A511**, 59 (1990).

[25] Y. Blumenfeld et al., *Phys. Rev. Lett.* **66**, 576 (1991).

[26] D.R. Bowman et al., *Nucl. Phys.* **A523**, 386 (1991).

[27] D.R. Bowman et al., *Phys. Rev Lett.* **67**, 1527 (1991).

[28] Y.H. Chung, S.Y. Cho, and N.T. Porile, *Nucl. Phys.* **A533**, 170 (1991).

[29] D.N. Delis et al., *Nucl. Phys.* **A534**, 403 (1991).

[30] R.T. de Souza et al., *Phys. Lett.* **B268**, 6 (1991).

[31] T. Ethvignot et al., *Phys. Rev. C* **43**, R2035 (1991).

[32] Y.D. Kim et al., *Phys. Rev Lett.* **67**, 14 (1991).

[33] E. Plasecki et al., *Phys. Rev. Lett.* **66**, 1291 (1991).

[34] J.L. Wile et al., *Phys. Lett.* **B264**, 26 (1991).

[35] J.L. Wile et al., *Phys. Rev. C* **45**, 2300 (1992).

[36] P. Roussel-Chomaz et al., *Nucl. Phys.* **A551**, 508 (1993).

[37] D.R. Bowman, Thesis, University of California at Berkeley, Lawrence Berkeley Laboratory report number LBL-27691 (1989).

[38] K. Hanold, L.G. Moretto, G.F. Peaslee, G.J. Wozniak, D.R. Bowman, M.F. Mohar, and D.J. Morrissey, *Phys. Rev. C* **48**, 723 (1993).

[39] W.L. Kehoe, Thesis, Univ. of Maryland, report number DOE/ER/40321-5 (1989).

[40] B.M. Sherrill, W. Benenson, D. Mikolas, D.J. Morrissey, J.A. Nolen Jr, and J.A. Winger, *Nucl. Instr. Meth.* **B56/57**, 1106 (1991).

[41] M.F. Mohar et al., *Phys. Rev. Lett.* **66**, 1571 (1991).

[42] D. Bazin et al., *Nucl. Phys.* **A515**, 349 (1990).

[43] D.J. Vieira, G.W. Butler, J.M. Wouters, and D.S. Brenner, *Annual Report Progress at LAMPF* p.192 (1984).

[44] M.A. McMahan et al., *Nucl. Instr. Meth.* **A253**, 1 (1986).

[45] F. Hubert, A. Fleury, R. Bimbot, and D. Gardes, *Ann. de Physique* **5**, 1 (1980).

[46] N.A. Orr et al., *Phys. Rev. Lett.* **69**, 2050 (1992).

[47] B.M. Sherrill, private communication (1993).

[48] K.A. Hanold, Thesis, University of California at Berkeley, Lawrence Berkeley Laboratory report number LBL-36087 (1994).

[49] S.J. Yennello, J.A. Winger, T. Antaya, W. Benenson, M.F. Mohar, D.J. Morrissey, N.A. Orr, and B.M. Sherrill, *Phys. Rev. C* **46**, 2620 (1992).

[50] A. Lleres, Thesis, L'University Scientifique Technologique et Medicale de Grenoble (1988).

[51] J.A. Winger et al., *Phys. Rev. C* **48**, 3097 (1993).

[52] D.J. Morrissey, private communication.

[53] M. Lewitowicz et al., *Nouvelles du GANIL* **48**, 7 (1993).

[54] G.F. Peaslee, private communication (1993).

[55] M. Colonna, P. Roussel-Chomaz, N. Colonna, M. Di Toro, L.G. Moretto, and G.J. Wozniak, *Phys. Lett.* **283**, 180 (1992).

[56] M. Colonna, M. Di Toro, V. Lataora, and N. Colonna, *Nucl. Phys.* **A545**, 111 (1992) and *Nucl. Phys.* **A541**, 295 (1992).

[57] D.R. Bowman et al., *Phys. Rev. C* **46**, 1824 (1992).

[58] H. Hauser and H. Feshbach, *Phys. Rev.* **87**, 336 (1952).

[59] L.G. Moretto, *Nucl. Phys.* **A247**, 211 (1975).

[60] L. Tassan-Got, private communication (1993).

[61] P. Möller and J.R. Nix, *Nucl. Phys.* **A361**, 117 (1981).

[62] A. Bonasera, G.F. Burgio, and M. DiToro, *Phys. Lett.* **B221**, 233 (1989)

[63] A. Bonasera, G. Russo, and H.H. Wolter, *Phys. Lett.* **B246**, 337 (1990).

FIGURES

FIG. 1. Schematic layout of the A1200 mass separator.

FIG. 2. Measured Z versus time of flight for the 50 MeV/nucleon ^{129}Xe + Al reaction.

FIG. 3. The top frame shows the typical Z resolution obtained in the 40 MeV/nucleon ^{129}Xe + Al reaction, while the middle frame shows the typical q resolution, and the bottom frame shows the typical A resolution.

FIG. 4. Momentum distribution for ^{104}Sn from the 40 MeV/nucleon ^{129}Xe + Al reaction shown as a solid line. The distributions for each charge state are shown in various textures.

FIG. 5. The angular acceptance of the A1200 is shown in the top frame. Calculated angular distributions from the incomplete fusion model for selected elements are shown in the bottom frame.

FIG. 6. The continuous curves are momentum distributions for representative light, medium, and heavy isotopes of all elements from the 50 MeV/nucleon ^{129}Xe+Al reaction. The dashed curves are the results of a incomplete fusion model calculation. The arrow is at the momentum of the beam in each frame. The momentum of the center of mass for this system is 251.9 MeV/c/u.

FIG. 7. Momentum distributions for all isotopes of Sn and Mo for the 50 MeV/nucleon ^{129}Xe+Al reaction.

FIG. 8. Isotopic cross sections for the 50 MeV/nucleon reactions. The curves join the cross sections for all the isotopes of a given element. All curves, except that for Z=40, are offset from their neighbors by an order of magnitude so that they do not overlap.

FIG. 9. Isotopic cross sections for the 40 MeV/nucleon reactions. The curves join the cross sections for all the isotopes of a given element. All curves, except that for Z=40, are offset from their neighbors by an order of magnitude so that they do not overlap.

FIG. 10. Isotopic cross sections for the 26 MeV/nucleon reactions. The curves join the cross sections for all the isotopes of a given element. All curves, except that for Z=40, are offset from their neighbors by an order of magnitude so that they do not overlap.

FIG. 11. The three-dimensional surface of the isotopic cross sections are shown. Note the variation of the shape of the surface with target and bombarding energy. The axis going to the right represents A, that going to the left represents Z, and the vertical axis represents yield.

FIG. 12. Contour plots of the isotopic cross sections in the A versus Z plane. Filled squares indicate the positions of the stable isotopes. The stair-stepping line shows the proton-rich limit of the known isotopes. The dashed curve just to the proton-rich side of the stable isotopes is the result from an incomplete fusion calculation.

FIG. 13. The average A and the full width at half maximum (FWHM) of the A distribution for each element from the 50 MeV/nucleon ^{129}Xe + Be (solid), C (dashed), and Al (dotted) reactions. Note the independence of the average and width of the A distribution on the target. The stair-stepping line shows the proton-rich limit of the known isotopes. Filled squares represent the positions of the stable isotopes.

FIG. 14. Contour plots of the isotopic cross sections in the A versus Z plane. In all three panels, the filled squares represent the positions of the stable isotopes, the stair-stepping line shows the proton-rich limit of the known isotopes, and the diamonds on the proton-rich side of the stable isotopes are the average atomic number for each isobar from the reaction of C + Ag measured by Chung, Chu, and Porile. The top frame compares the results from the reactions of 50 MeV/nucleon ^{129}Xe + C and 45 MeV/nucleon ^{12}C + Ag, the middle frame contains the results of 40 MeV/nucleon ^{129}Xe + C and 35 MeV/nucleon ^{12}C + Ag, and the bottom frame shows the results from 26 MeV/nucleon ^{129}Xe + C and 25 MeV/nucleon ^{12}C + Ag.

FIG. 15. The mass yields from the 50 MeV/nucleon Xe+Al reaction are shown by the solid curves. The mass yields from the 70 MeV/nucleon ^{92}Mo+^{58}Ni reaction are indicated by the histograms.

FIG. 16. The measured elemental cross sections are shown as diamonds. Complex fragment cross sections from similar reactions are shown as pluses. Shown as a dotted line are the elemental cross sections from an incomplete fusion model calculation.

FIG. 17. The isobaric cross sections for each of the target-beam energy combinations from this work are shown by the curves. Also shown as pluses and times symbols are the cross sections from 30 MeV/nucleon ^{14}N + ^{124}Sn, 49 MeV/nucleon ^{12}C + ^{124}Sn, 30 MeV/nucleon ^{20}Ne + ^{124}Sn, 40 MeV/nucleon ^{20}Ne + ^{124}Sn, 49 MeV/nucleon ^{20}Ne + ^{124}Sn, 27 MeV/nucleon ^{40}Ar + ^{124}Sn, 35 MeV/nucleon ^{40}Ar + ^{124}Sn, and 44 MeV/nucleon ^{40}Ar + ^{124}Sn as indicated in each panel.

FIG. 18. Cross section contours in the Z–velocity plane for all systems measured in this work. Also shown are complex fragment ("CF") data from 26 MeV/nucleon ^{129}Xe+C and Al, 40 MeV/nucleon ^{139}La+C and Al, and 50 MeV/nucleon ^{129}Xe+C and Al. The upper horizontal line in each frame lies along the velocity of the beam. The lower horizontal line in each frame lies along the velocity of the center of mass for that system.

FIG. 19. Schematic representation of the effect of light charged-particle evaporation on the correlation between the velocity and the Z of the incomplete fusion product. Z_{proj} is the Z value of the projectile. The solid line represents the locus of the velocities of the primary products from an incomplete fusion process. The short horizontal arrow to the dotted line shows the effect of evaporation on these products for low bombarding energies. The dashed lines show the loci of the velocities of the products after evaporation for higher bombarding energies.

FIG. 20. The distribution of cross section as a function of Z value and velocity are shown in the first, third, and fifth rows. The second, fourth, and sixth rows show the prediction of the incomplete fusion calculation. The upper horizontal line in each frame corresponds to the velocity of the beam. The lower horizontal line in each frame corresponds to the velocity of the center of mass for that reaction.

FIG. 21. Experimental isotopic cross sections for the 50 MeV/nucleon ^{129}Xe + Al reaction are shown as solid curves. The predictions of the incomplete fusion calculation are shown as the dotted curves for the same reaction. The cross section for each element has been offset by an order of magnitude from its neighbors. The magnitude of the calculation has been scaled in this figure for easier comparison of the centroid values and the widths of the distributions with the data.

FIG. 22. The average masses of each element predicted by GEMINI for two different initial nuclei are shown. One system is very proton-rich, Z=67 and A=149 and is shown as a solid line. The other system is very neutron-rich, Z=67 and A=166 and is shown as a dotted line. Shown as the stair-stepping line is the proton-rich limit of the known isotopes. Solid squares mark the positions of the stable isotopes.

FIG. 23. The mass, excitation energy, and velocity of the primary projectile-like fragment as a function of impact parameter from both the BNV (dotted) and ICF (solid curve) models for the reaction of 50 MeV/nucleon ^{129}Xe + Al. The crosses with error bars are the results and uncertainties from the BNV calculation at each impact parameter.

FIG. 24. The upper left frame shows the cross sections in the Z versus velocity plane from the 50 MeV/nucleon ^{129}Xe + Al reaction. The upper horizontal line corresponds to the velocity of the beam. The lower horizontal line corresponds to the velocity of the center of mass. The upper right frame shows the same distribution predicted by the ICF calculation. The lower left frame shows the distribution predicted by the BNV calculation. The contour lines are linearly spaced. The lower right frame shows the elemental cross sections. The heavy residue cross sections from the current work are shown as diamonds; the ICF predictions, as a dashed line; and the BNV predictions, as a dotted line.

TABLES

TABLE I. Maximum excitation energy possible for each beam energy and target combination (in MeV).

Beam Energy/Target	Be	C	Al
26 MeV/nucleon	220	285	580
40	335	440	890
50	420	550	1115

TABLE II. Excitation energy and average residue Z value for the transfer of a ^{6}Li to form ^{135}La in the ^{129}Xe + Al reaction.

Beam Energy (E/A)	Excitation Energy (MeV)	Average Residue Z Value
26 MeV	175	53.5
40	250	52.0
50	310	50.8

TABLE III. Excitation energy and average residue Z value for the transfer of a ^{12}C to form ^{141}Nd in the ^{129}Xe + Al reaction.

Beam Energy (E/A)	Excitation Energy (MeV)	Average Residue Z Value
26 MeV	320	53.6
40	470	50.6
50	580	48.2

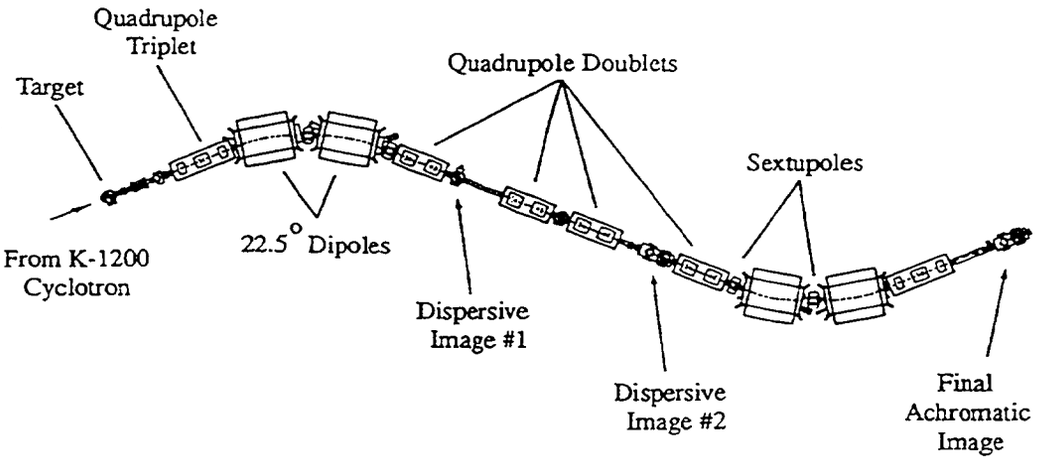
Quadrupole
Triplet
Target
Quadrupole Doublets
Sextupoles
From K-1200
Cyclotron
22.5° Dipoles
Dispersive
Image #1
Dispersive
Image #2
Final
Achromatic
Image

Fig. 1

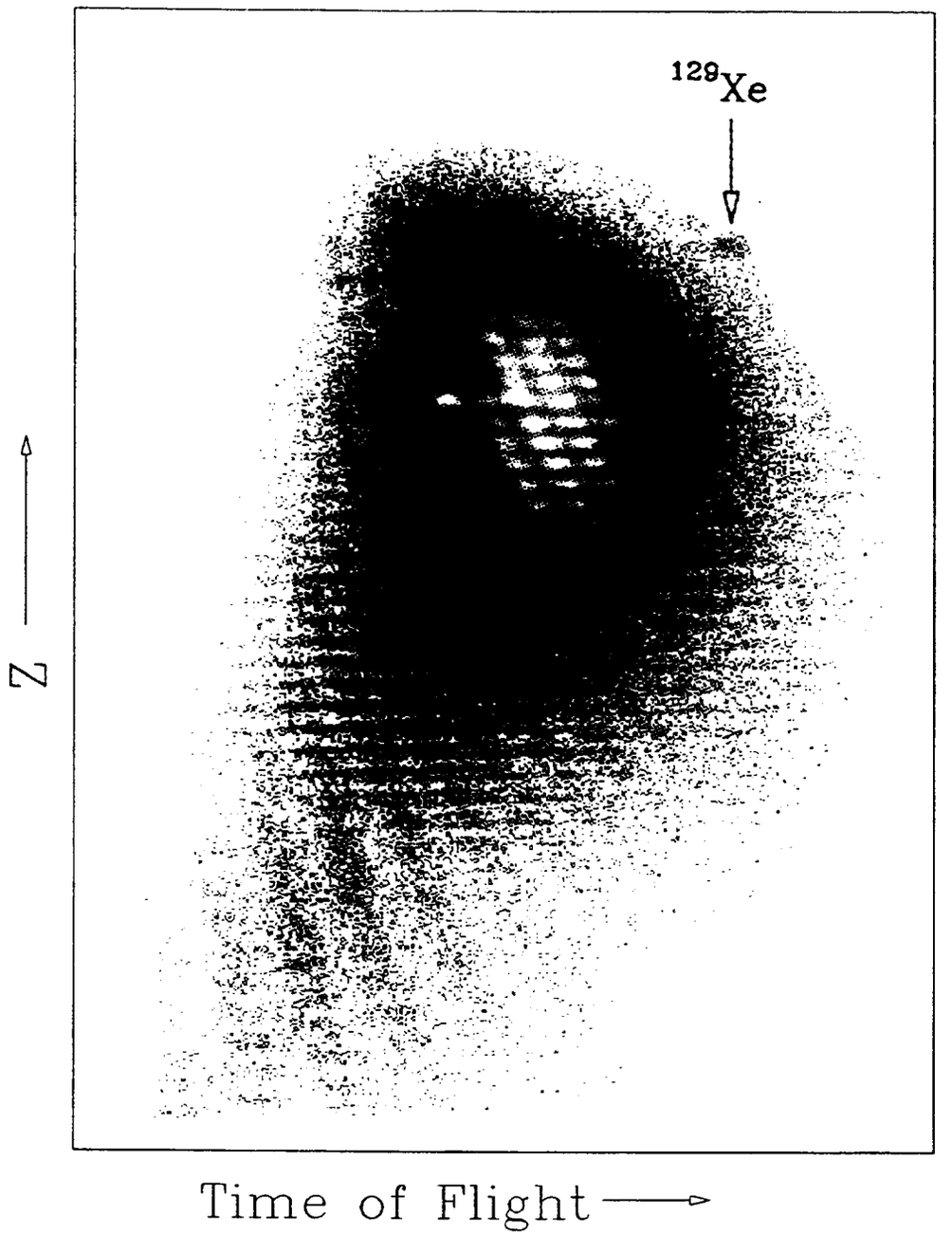

Figure 2.4: Measured Z versus time of flight for the 50 MeV/nucleon ^{129}Xe + Al reaction.

Fig. 2

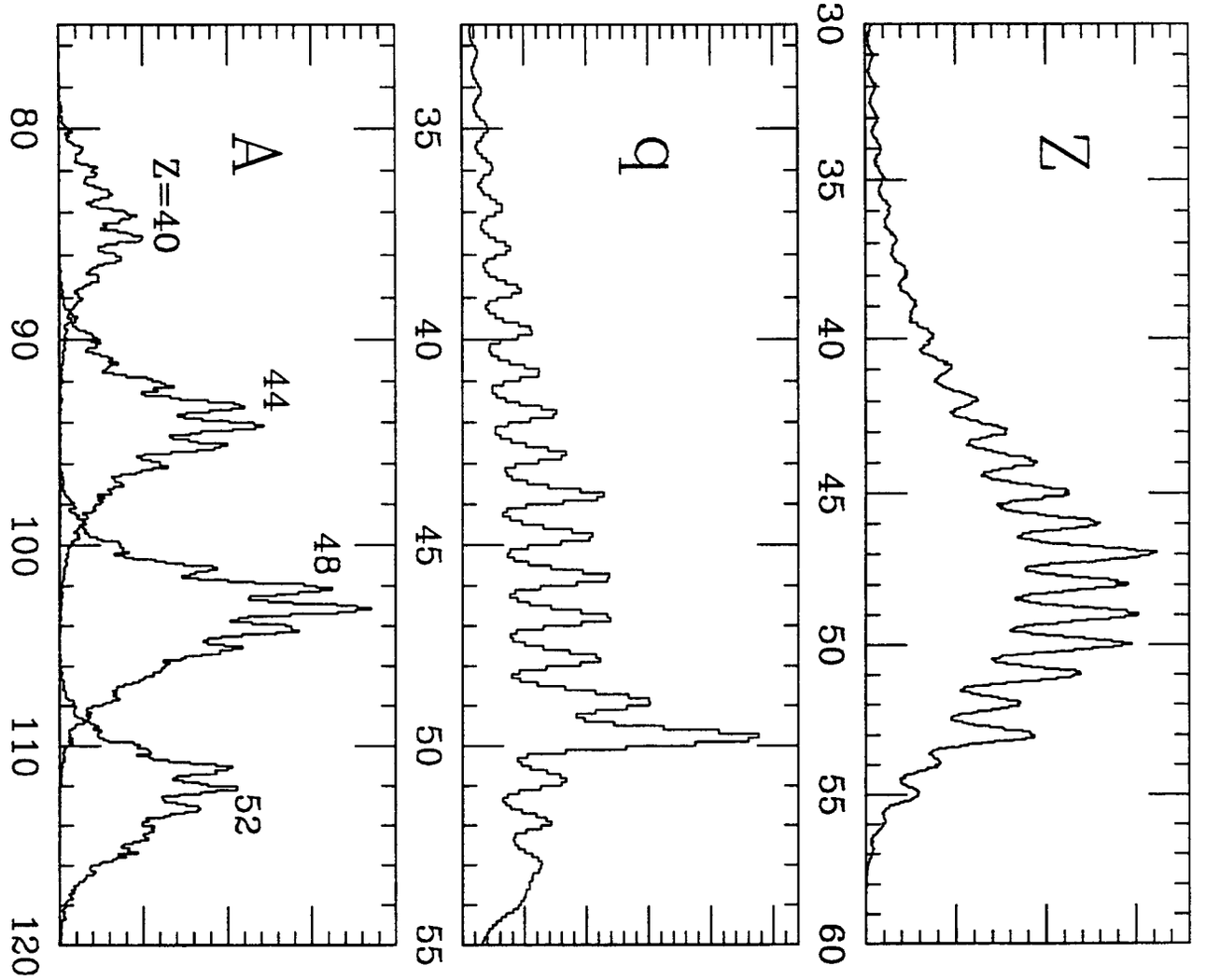

Fig. 3

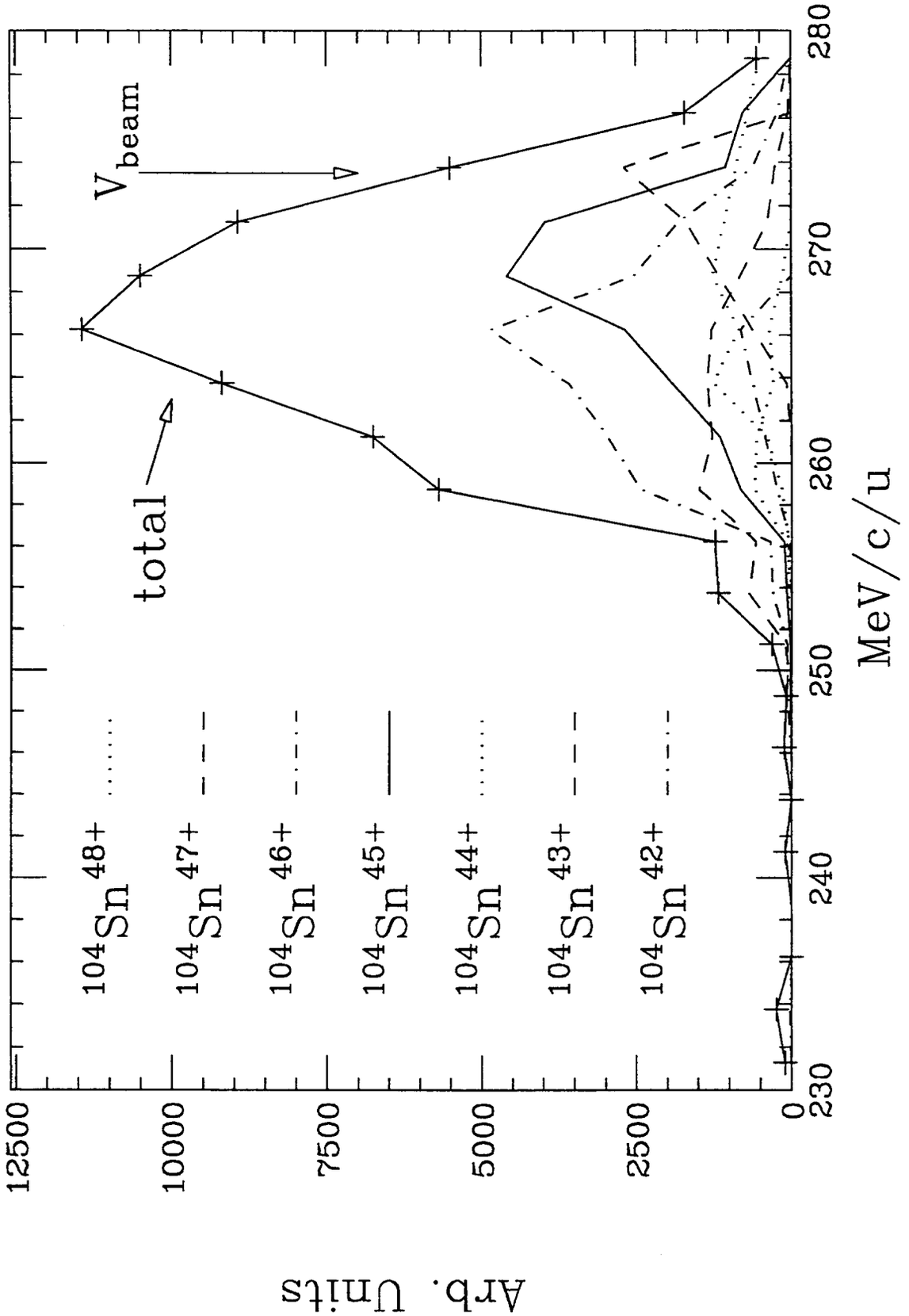
Arb. Units
12500
10000
7500
5000
2500
0
230
240
250
260
270
280
MeV/c/u
V_{beam}
total
$^{104}Sn^{48+}$
$^{104}Sn^{47+}$
$^{104}Sn^{46+}$
$^{104}Sn^{45+}$
$^{104}Sn^{44+}$
$^{104}Sn^{43+}$
$^{104}Sn^{42+}$

Fig. 4

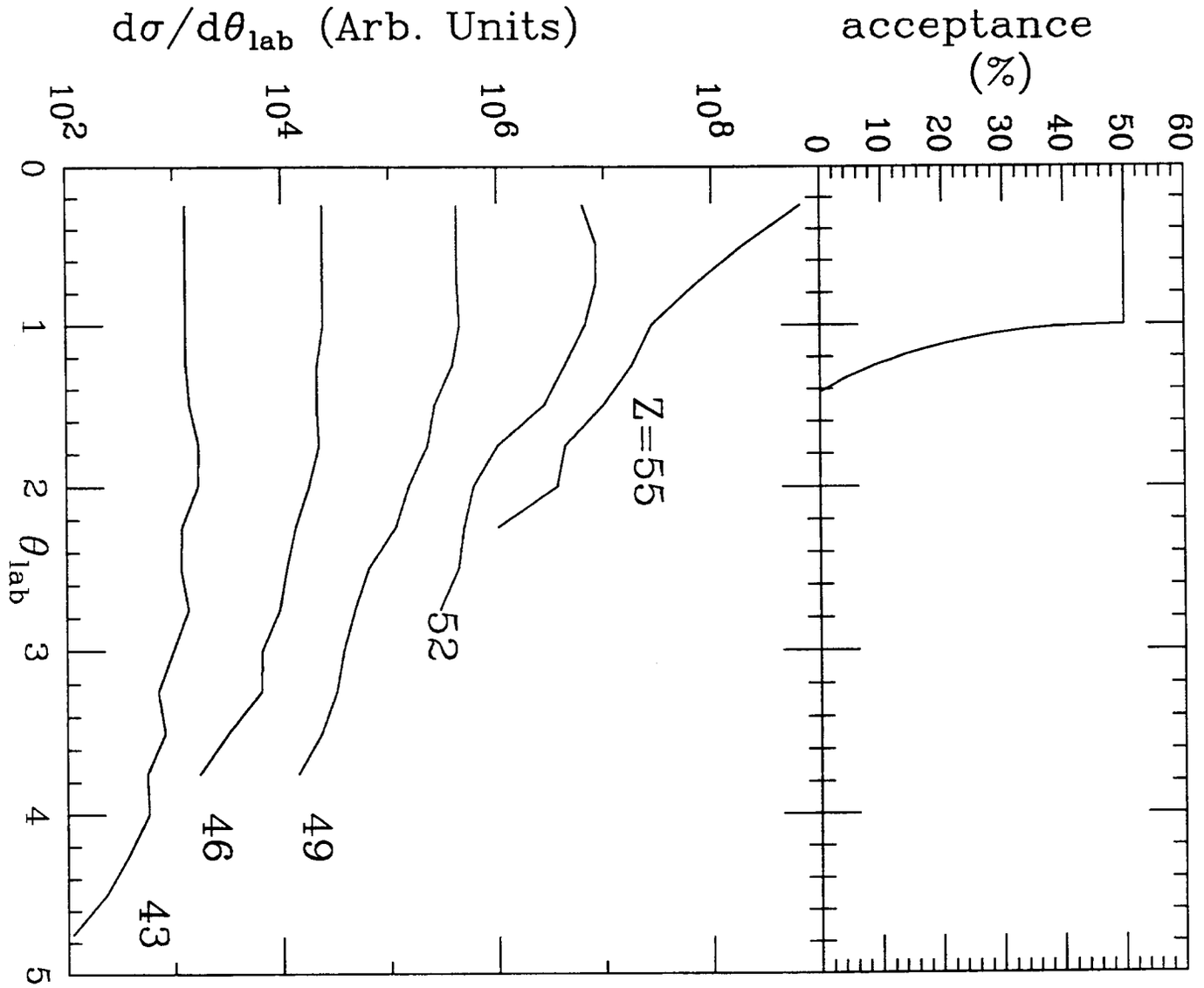
dσ/dθlab (Arb. Units)
acceptance
(%)
10^2
10^4
10^6
10^8
0
10
20
30
40
50
60
0
1
2
θlab
3
4
5
Z=55
52
49
46
43

Fig. 5

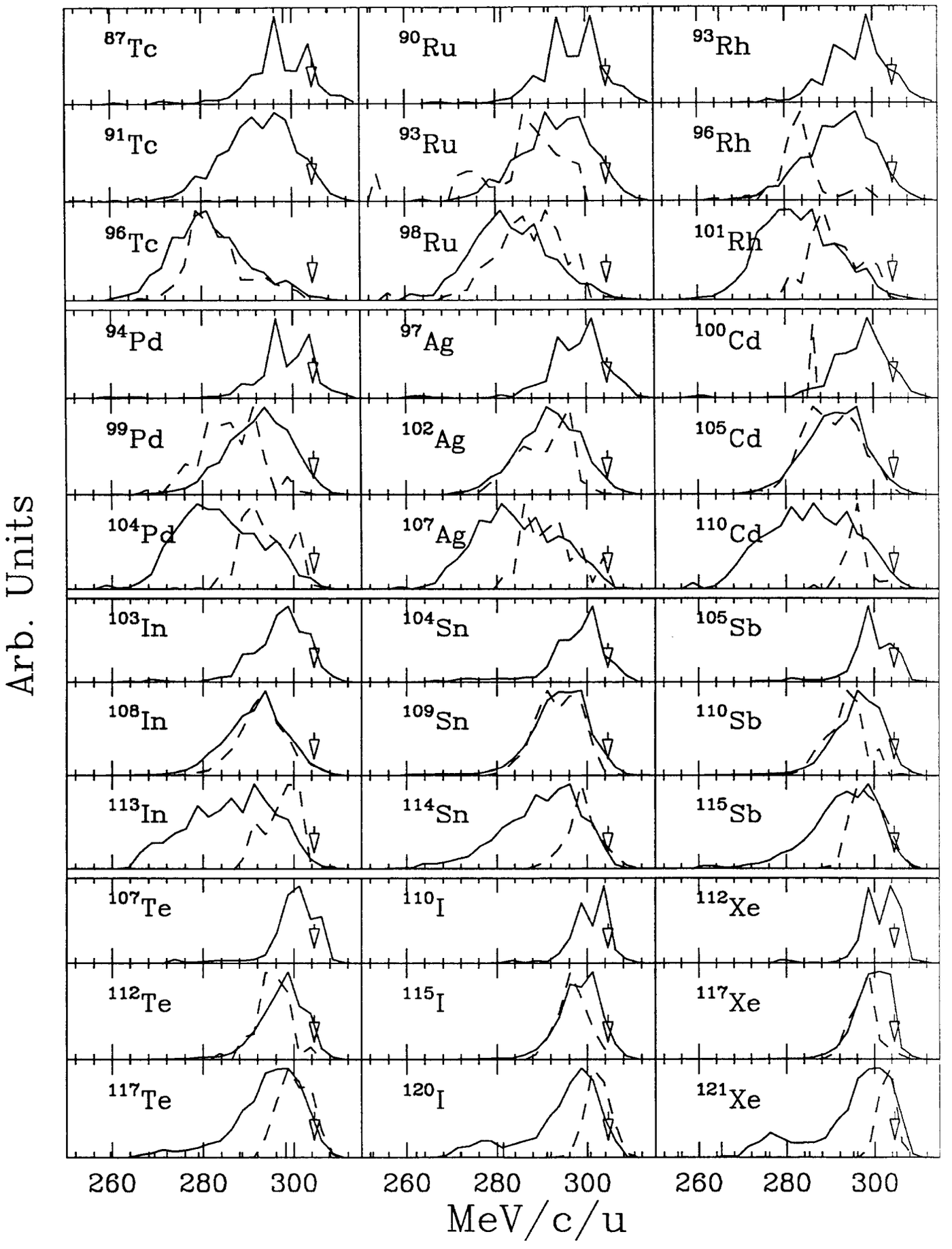
^{87}Tc
^{90}Ru
^{93}Rh
^{91}Tc
^{93}Ru
^{96}Rh
^{96}Tc
^{98}Ru
^{101}Rh
^{94}Pd
^{97}Ag
^{100}Cd
^{99}Pd
^{102}Ag
^{105}Cd
^{104}Pd
^{107}Ag
^{110}Cd
^{103}In
^{104}Sn
^{105}Sb
^{108}In
^{109}Sn
^{110}Sb
^{113}In
^{114}Sn
^{115}Sb
^{107}Te
^{110}I
^{112}Xe
^{112}Te
^{115}I
^{117}Xe
^{117}Te
^{120}I
^{121}Xe
Arb. Units
260
280
300
260
280
300
260
280
300
MeV/c/u

Fig. 6

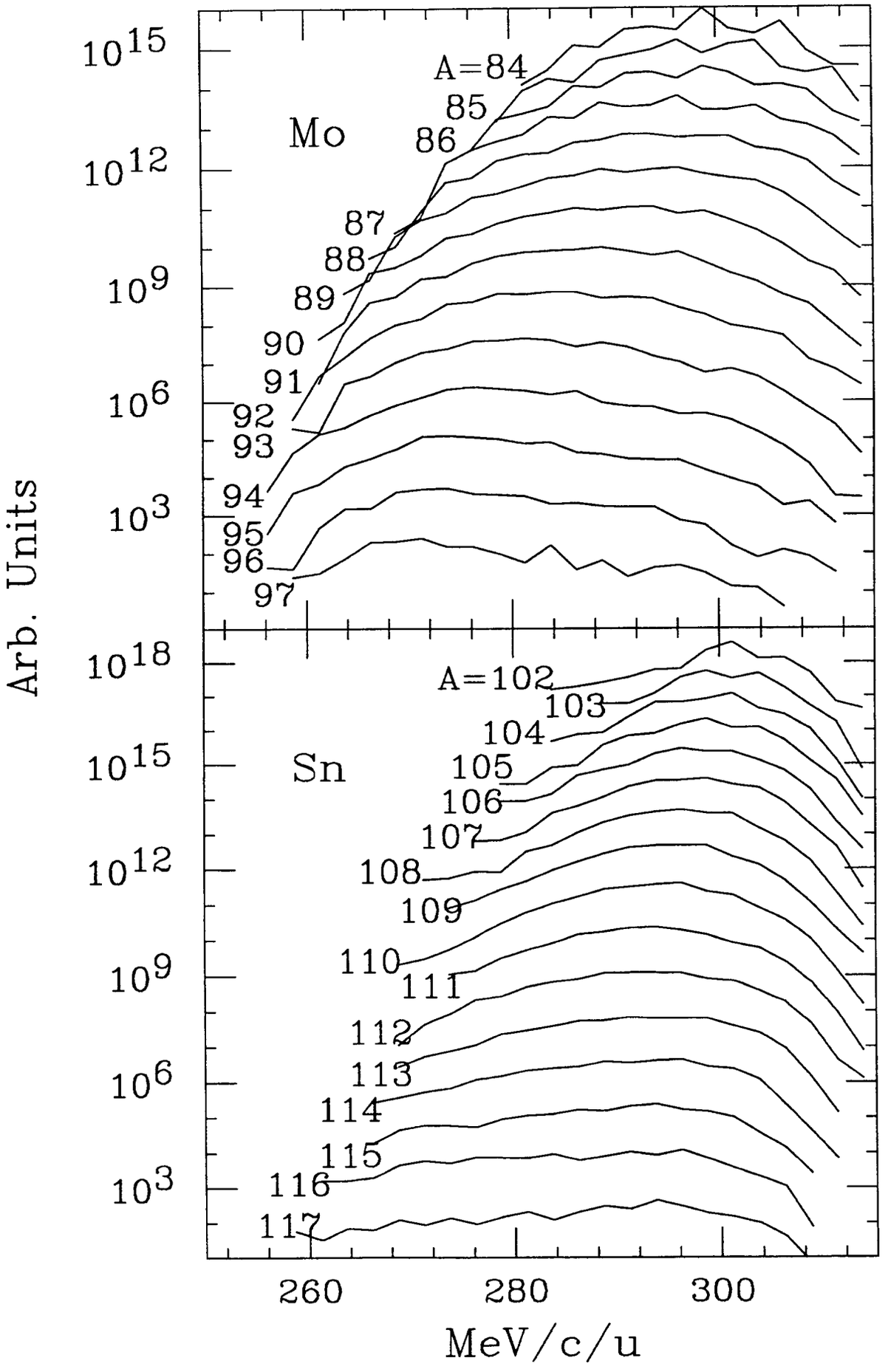
Arb. Units
10^{15}
10^{12}
10^{9}
10^{6}
10^{3}
Mo
A=84
85
86
87
88
89
90
91
92
93
94
95
96
97
10^{18}
10^{15}
10^{12}
10^{9}
10^{6}
10^{3}
Sn
A=102
103
104
105
106
107
108
109
110
111
112
113
114
115
116
117
260
280
300
MeV/c/u

Fig. 7

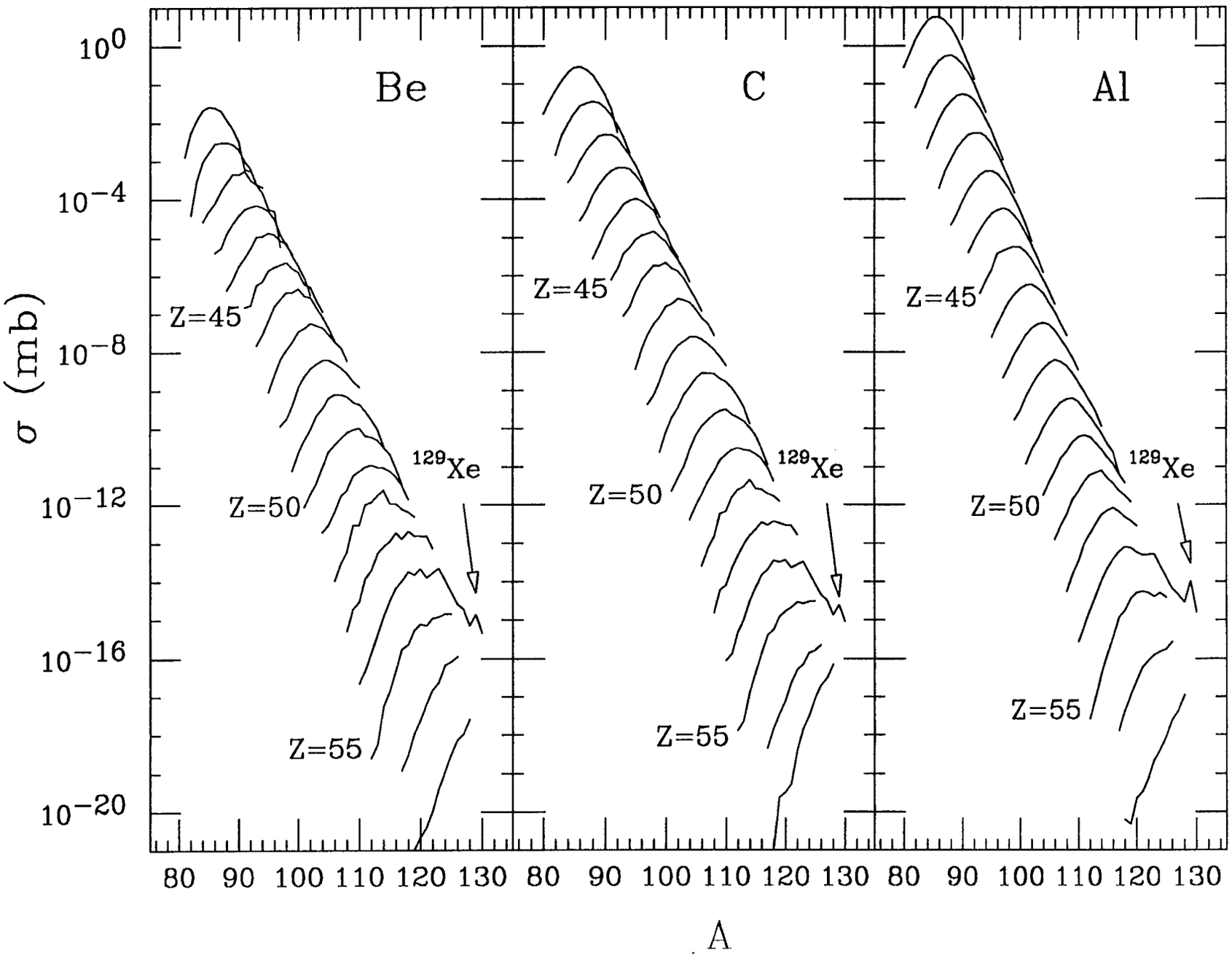
Be
C
Al
Z=45
Z=50
Z=55
^{129}Xe
10^{0}
10^{-4}
10^{-8}
10^{-12}
10^{-16}
10^{-20}
σ (mb)
80 90 100 110 120 130
A

Fig. 8
54

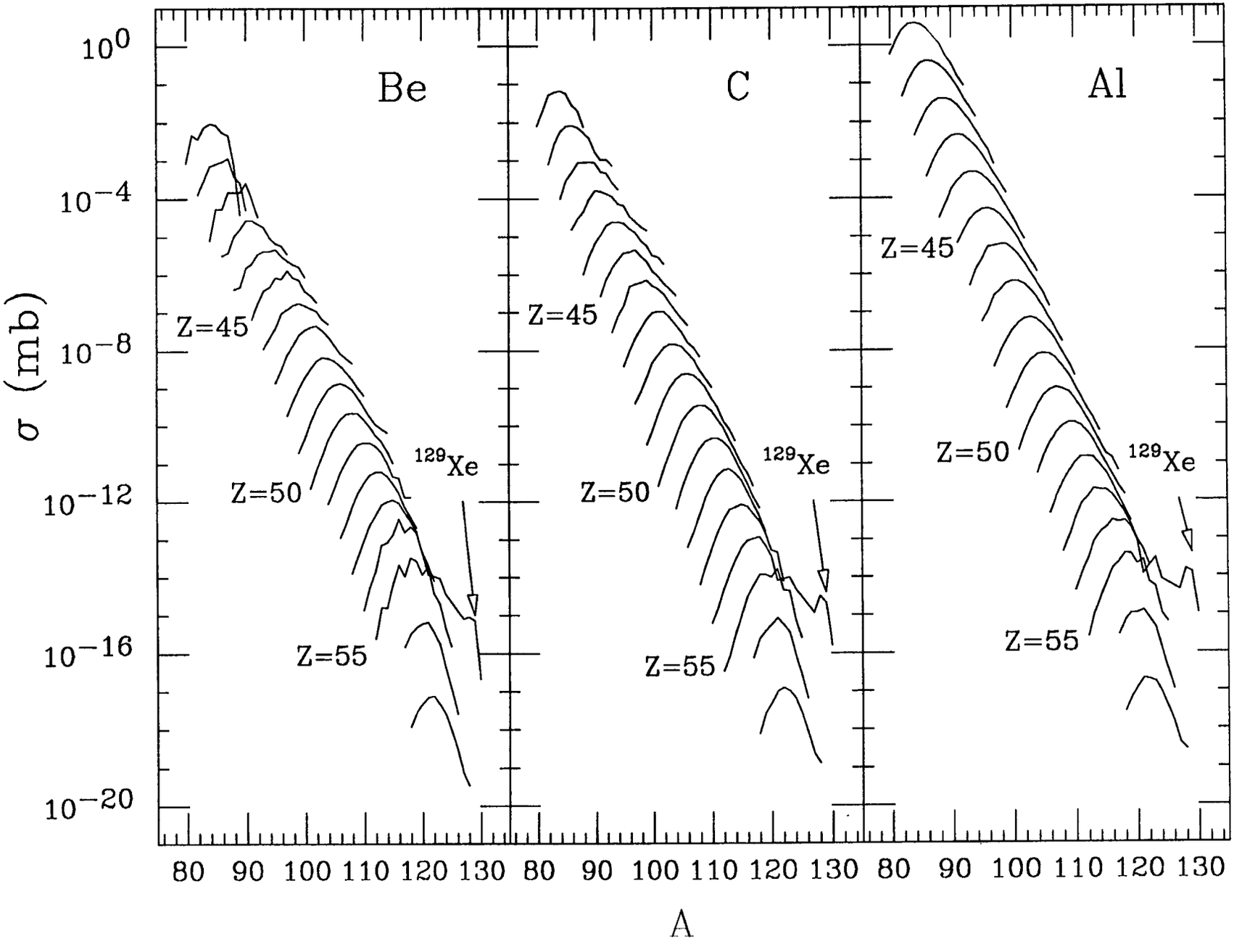
Be
C
Al
Z=45
Z=50
Z=55
^{129}Xe
10^{0}
10^{-4}
10^{-8}
10^{-12}
10^{-16}
10^{-20}
σ (mb)
80 90 100 110 120 130
A

Fig. 9
55

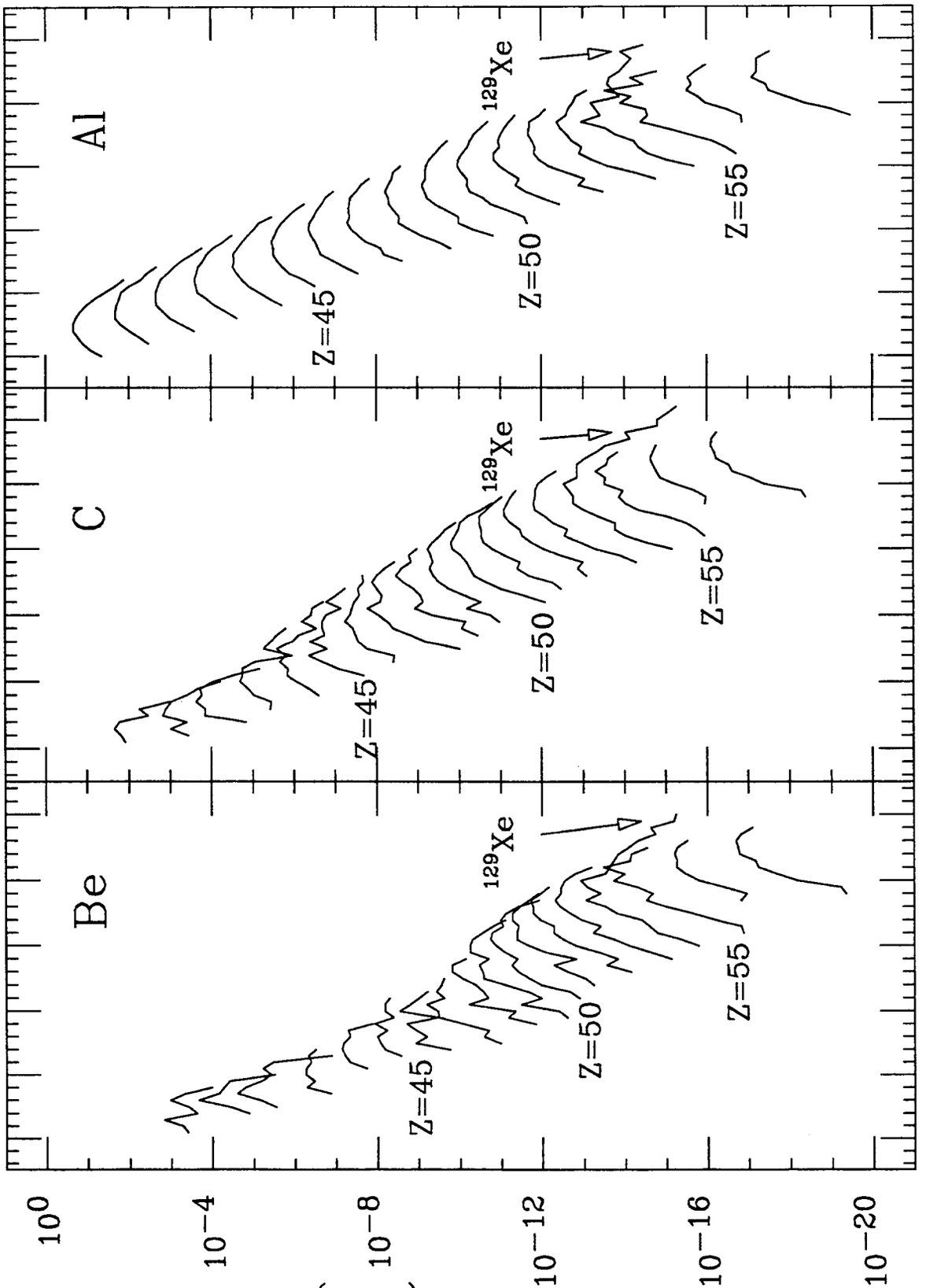

Fig. 10

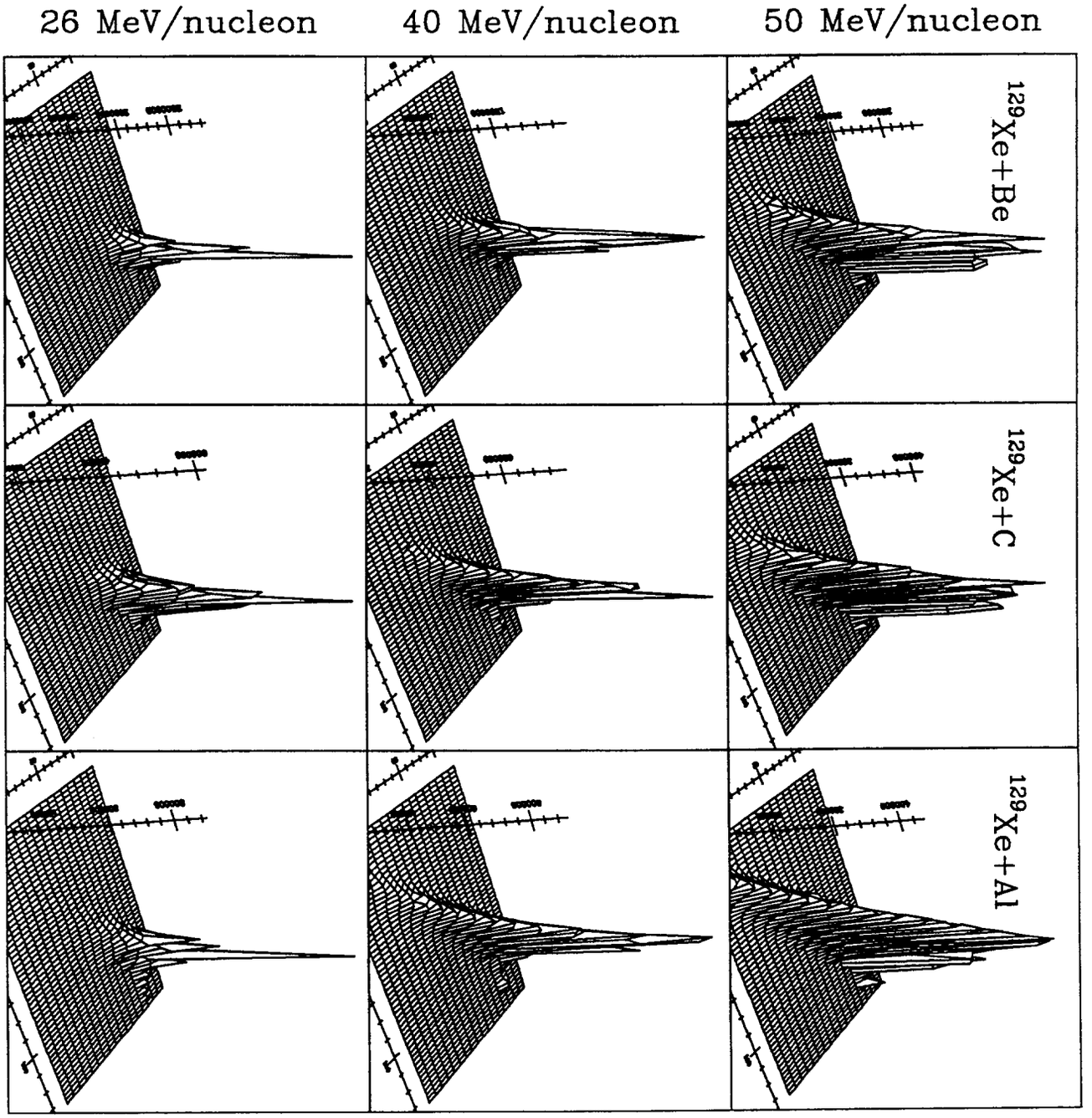
26 MeV/nucleon
40 MeV/nucleon
50 MeV/nucleon
^{129}Xe+Be
^{129}Xe+C
^{129}Xe+Al

Fig. 11

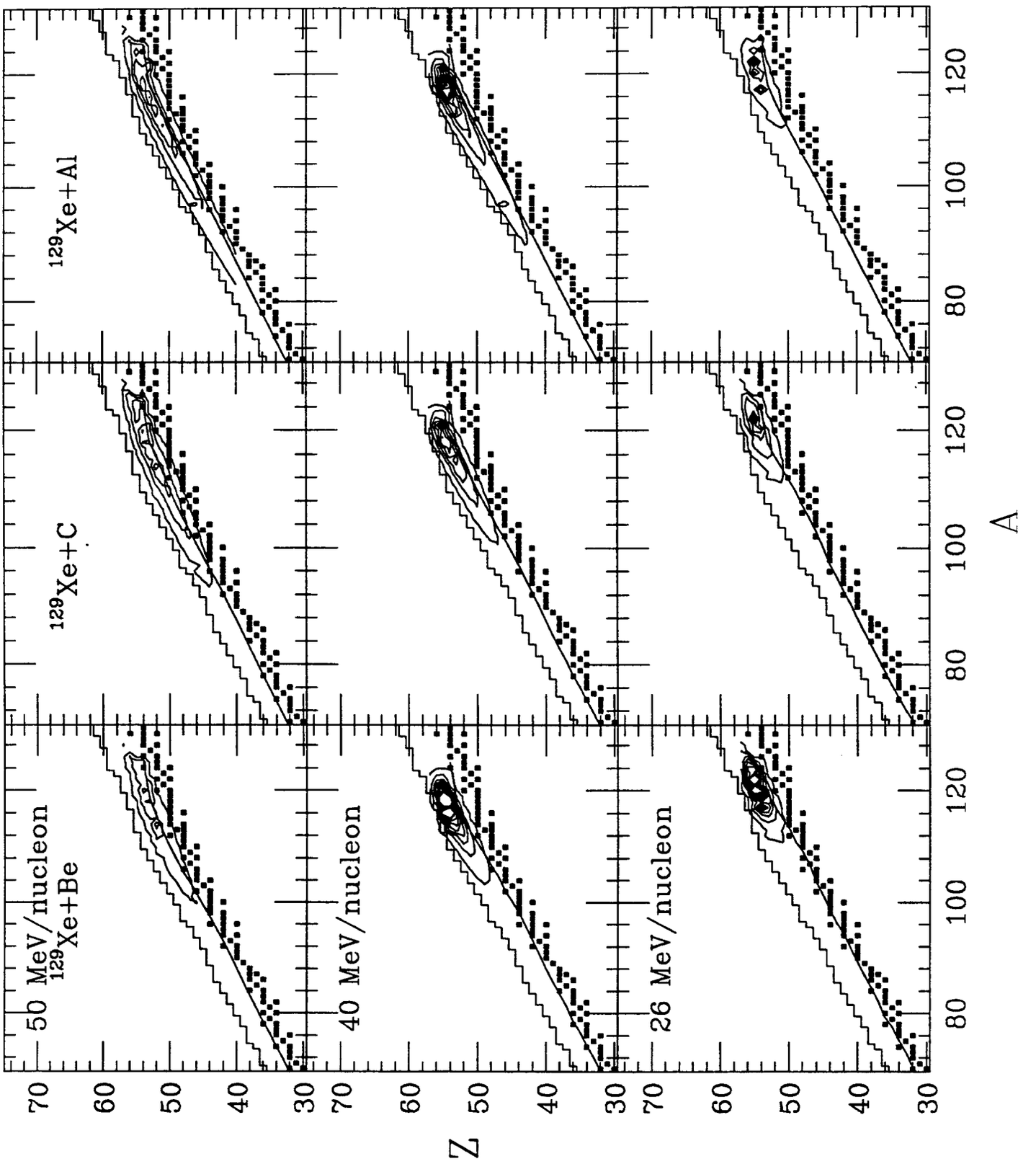
50 MeV/nucleon
^{129}Xe+Be
^{129}Xe+C
^{129}Xe+Al
40 MeV/nucleon
26 MeV/nucleon
Z
A
70
60
50
40
30
80
100
120

Fig. 12

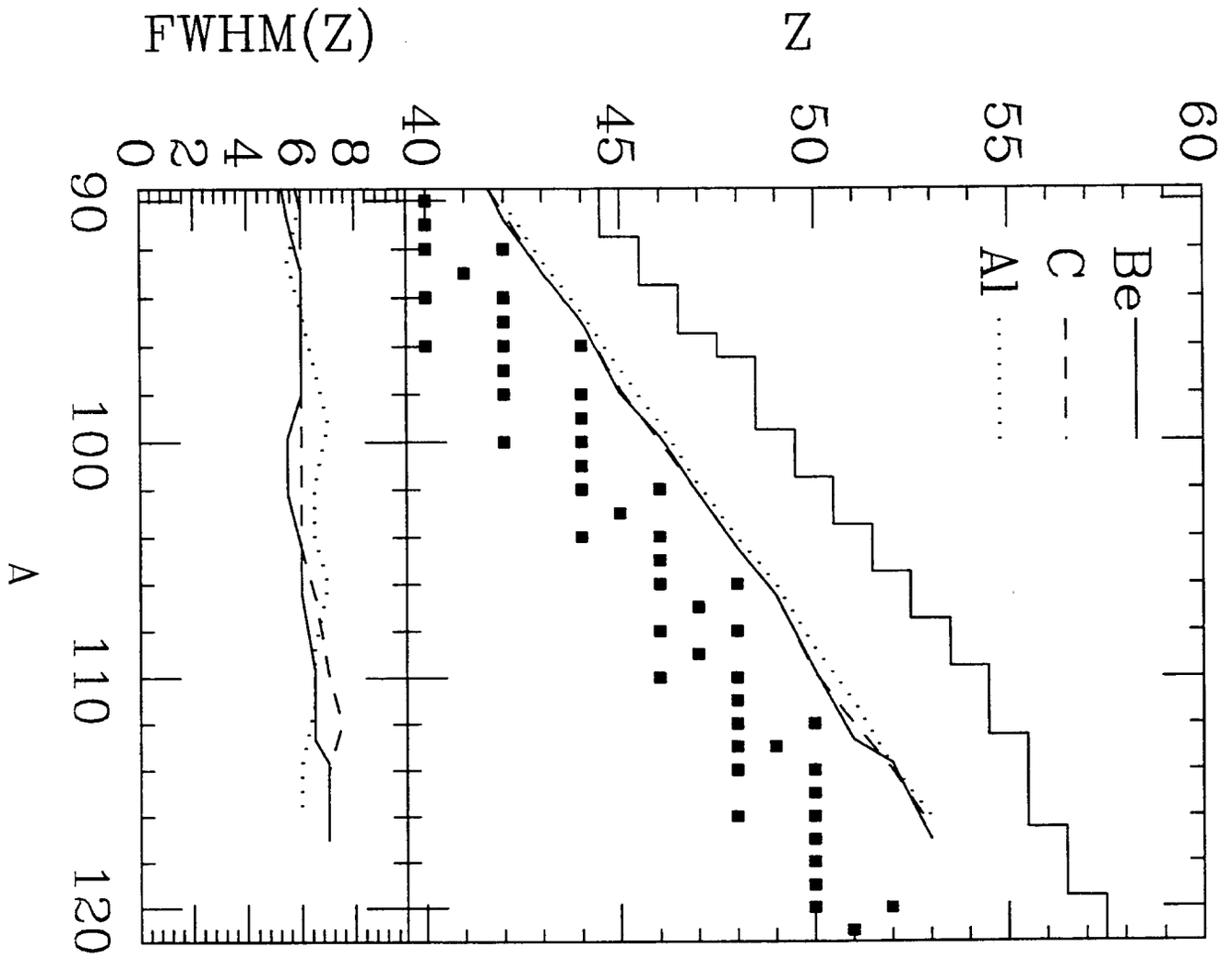

Fig. 13

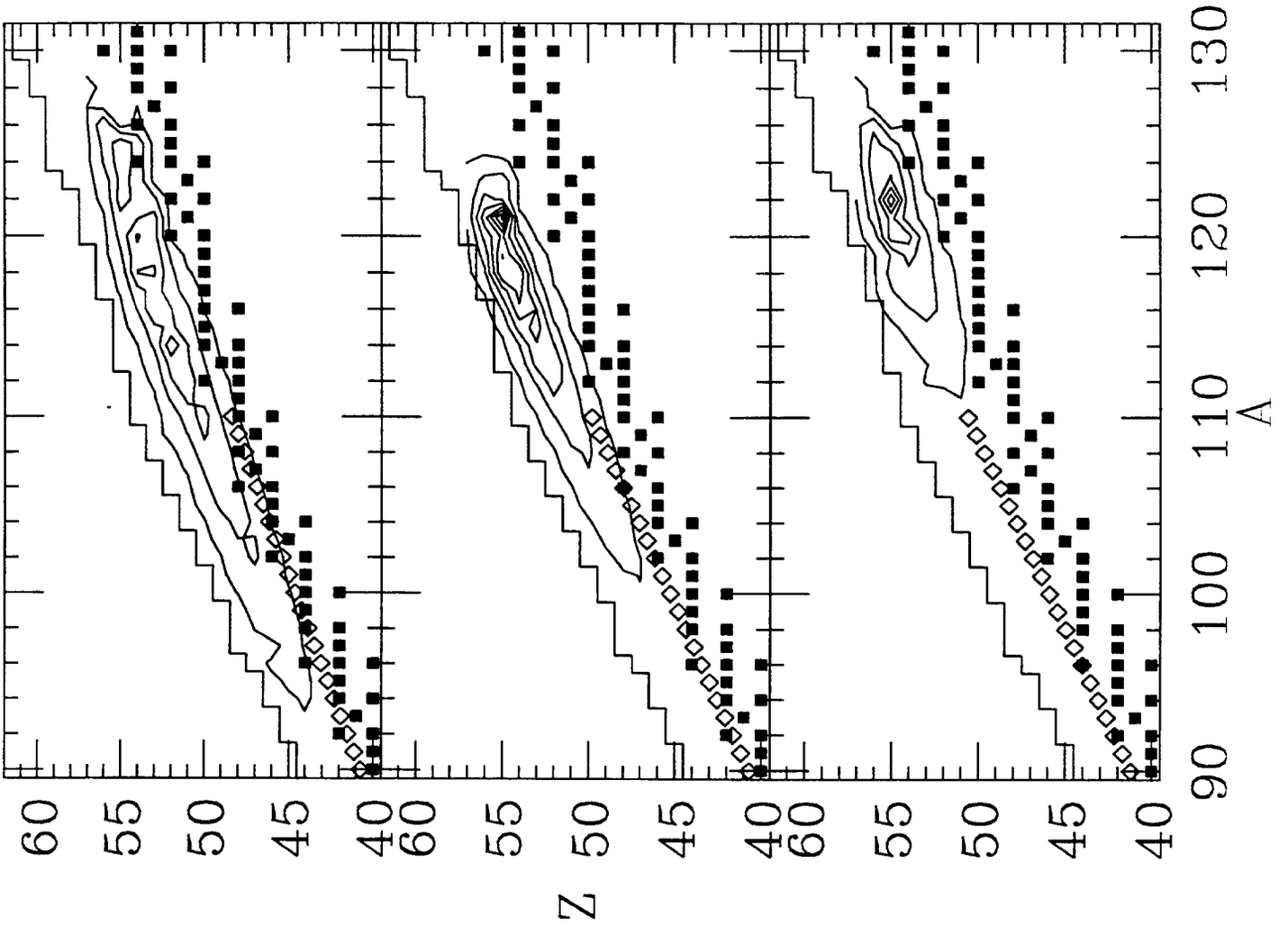

Fig. 14

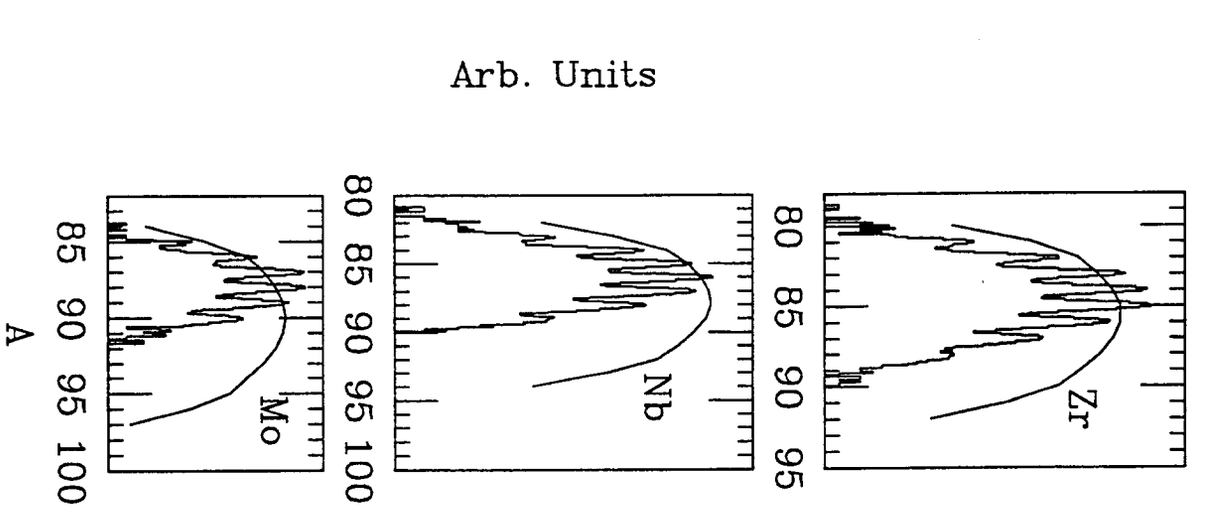

Fig. 15

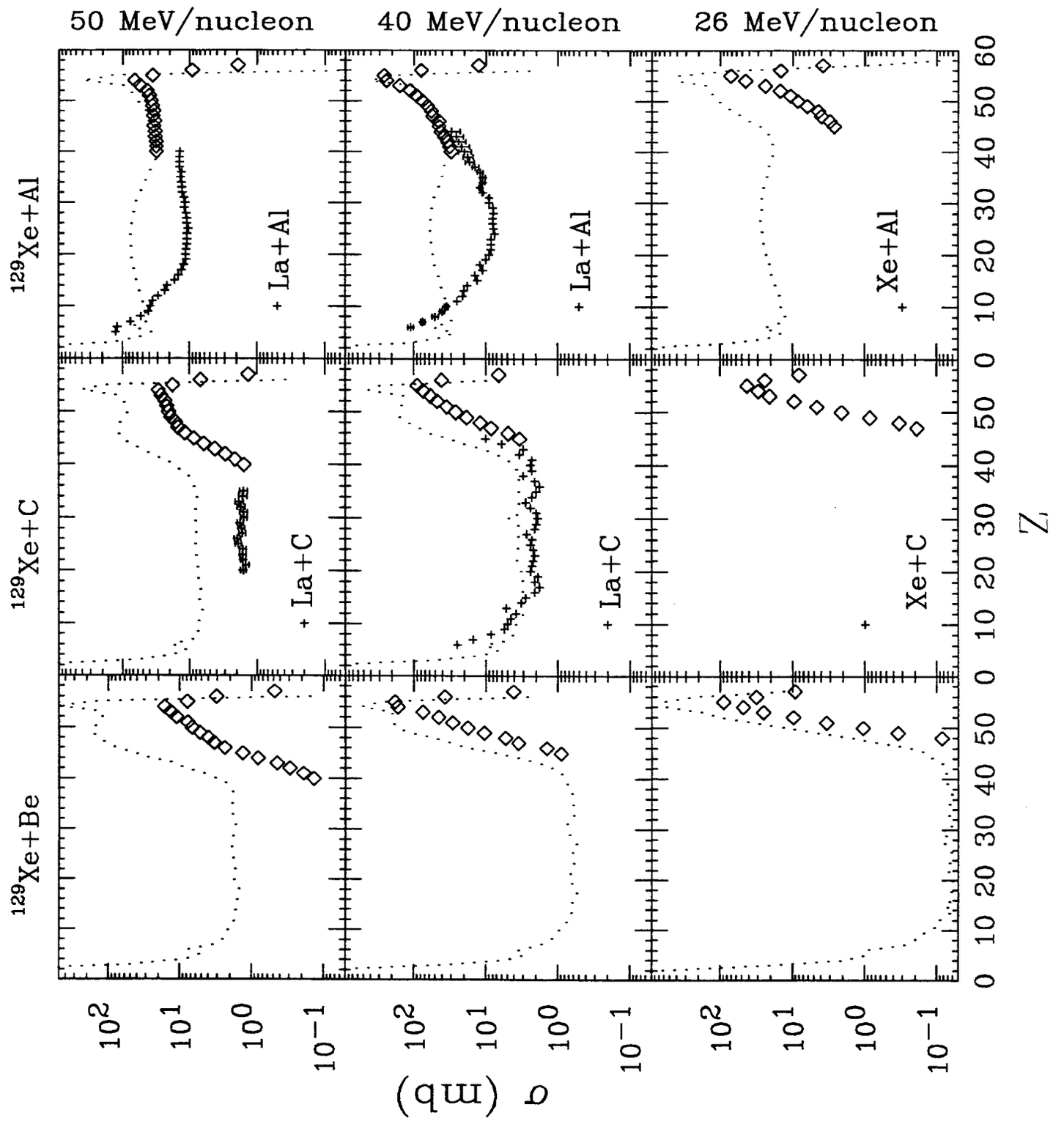
50 MeV/nucleon
40 MeV/nucleon
26 MeV/nucleon
^{129}Xe+Al
^{129}Xe+C
^{129}Xe+Be
+ La+Al
+ La+C
+ Xe+Al
+ Xe+C
σ (mb)
Z

Fig. 16

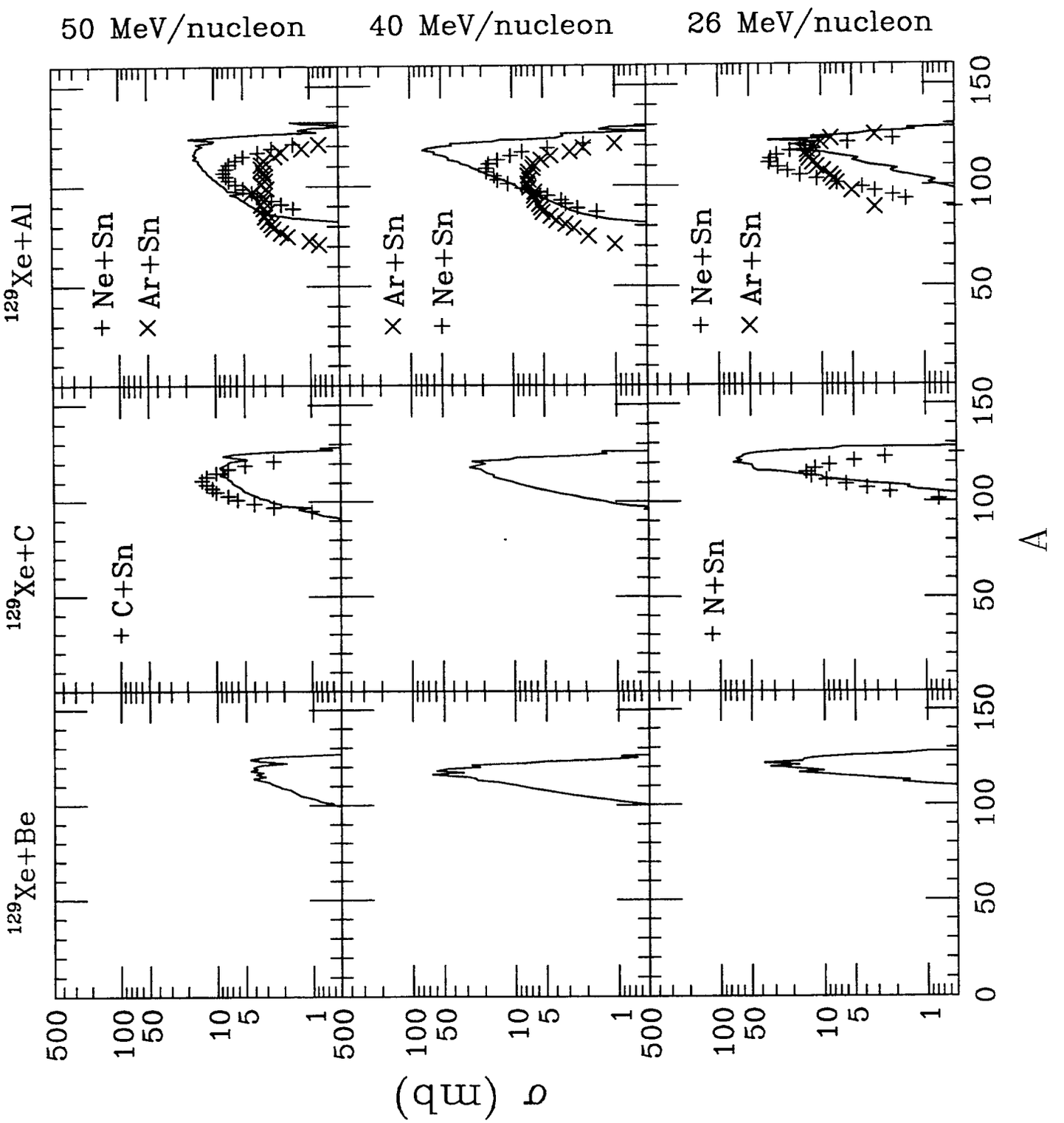
50 MeV/nucleon
40 MeV/nucleon
26 MeV/nucleon
^{129}Xe+Al
^{129}Xe+C
^{129}Xe+Be
+ Ne+Sn
× Ar+Sn
+ C+Sn
+ N+Sn
σ (mb)
A

Fig. 17

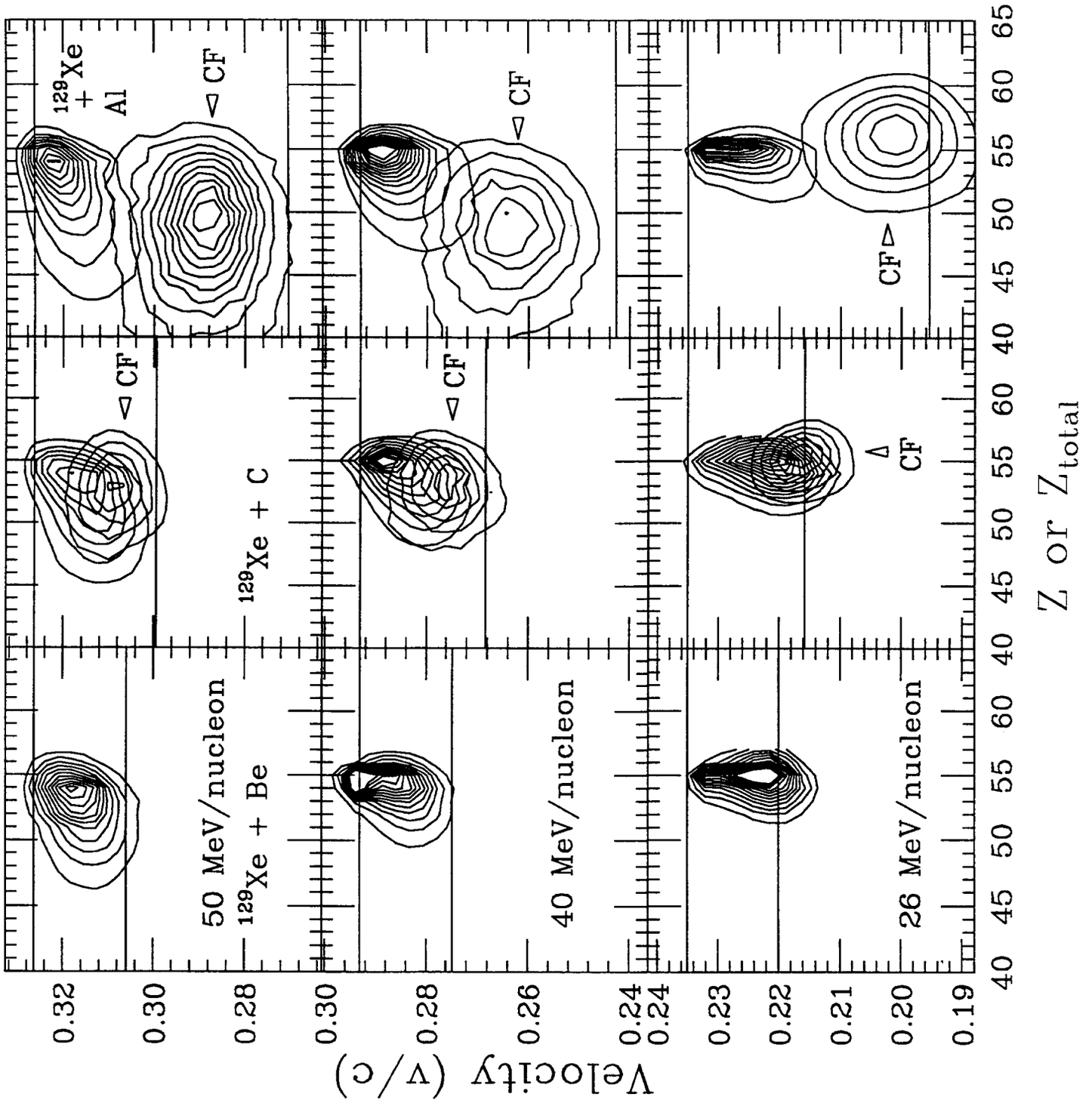
Velocity (v/c)
Z or Z_{total}
50 MeV/nucleon
40 MeV/nucleon
26 MeV/nucleon
^{129}Xe + Be
^{129}Xe + C
^{129}Xe + Al
CF
CF
CF
CF
CF
CF

Fig. 18

Velocity
V_{beam}
V_{cm}
high E
medium E
low E
Z_{proj}
$Z_{proj}+Z_{target}$
Z

Fig. 19

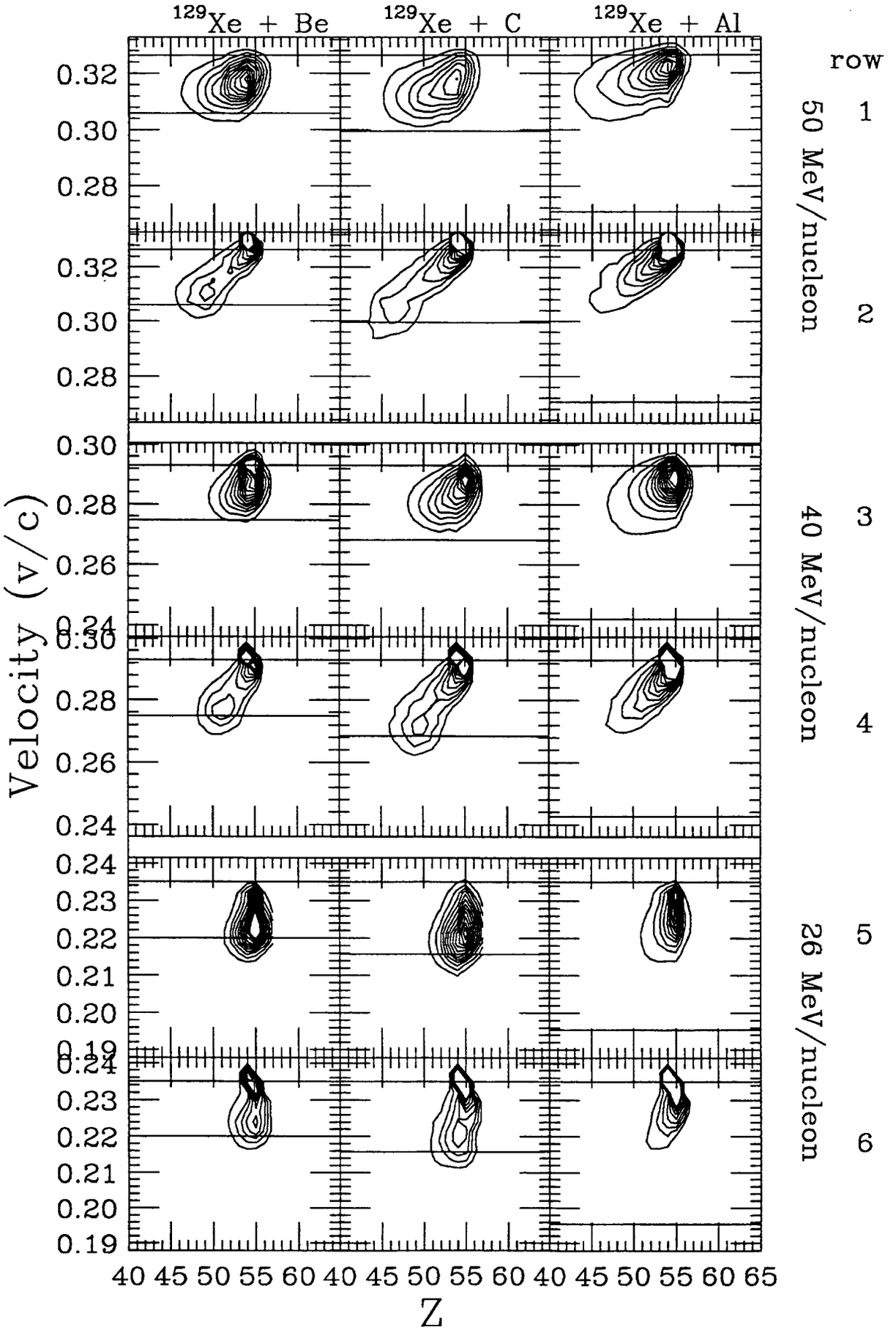
^{129}Xe + Be
^{129}Xe + C
^{129}Xe + Al
row
50 MeV/nucleon
40 MeV/nucleon
26 MeV/nucleon
1
2
3
4
5
6
Velocity (v/c)
0.32
0.30
0.28
0.26
0.24
0.23
0.22
0.21
0.20
0.19
40 45 50 55 60 40 45 50 55 60 40 45 50 55 60 65
Z

Fig. 20

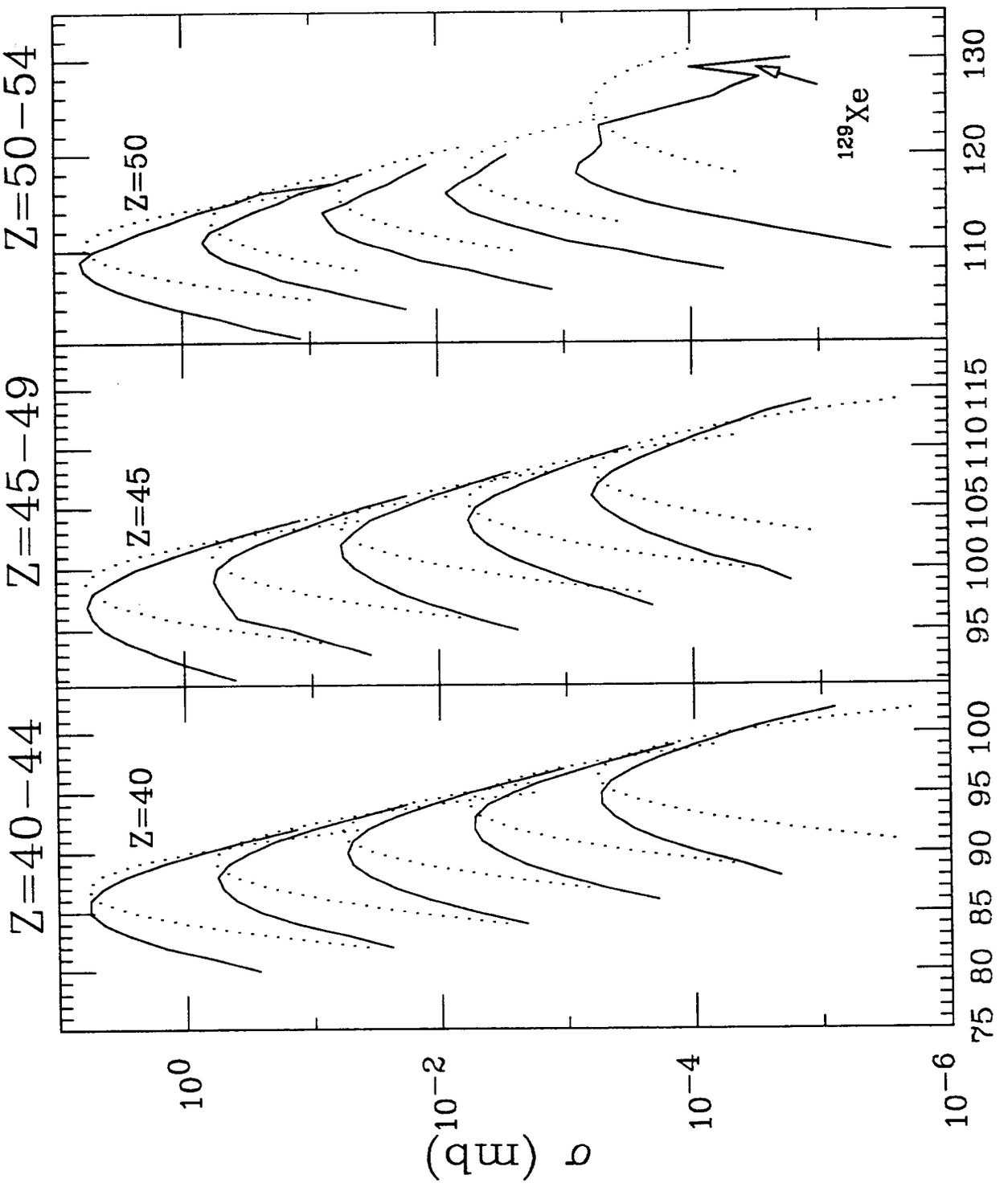

Fig. 21

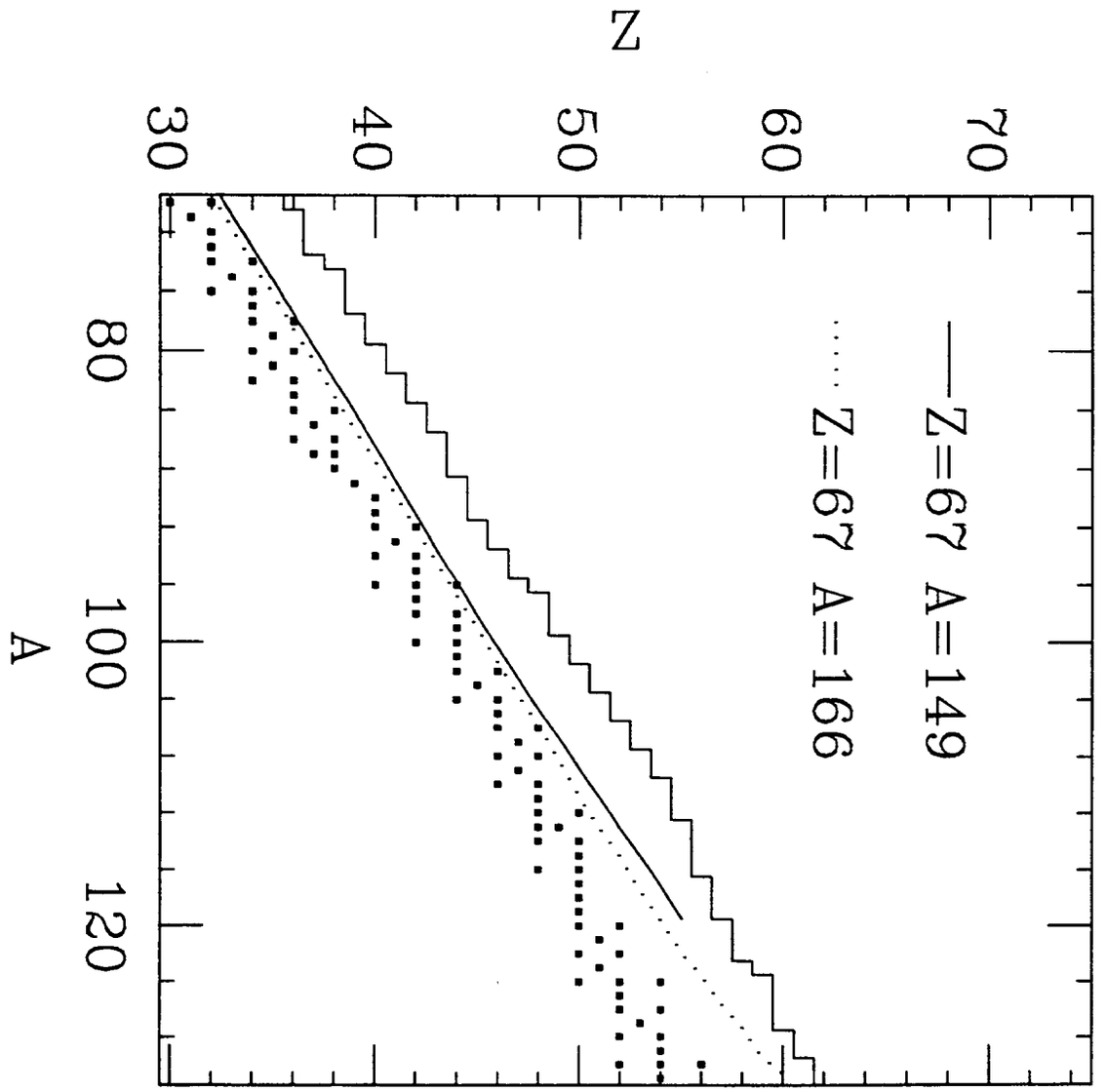

Fig. 22

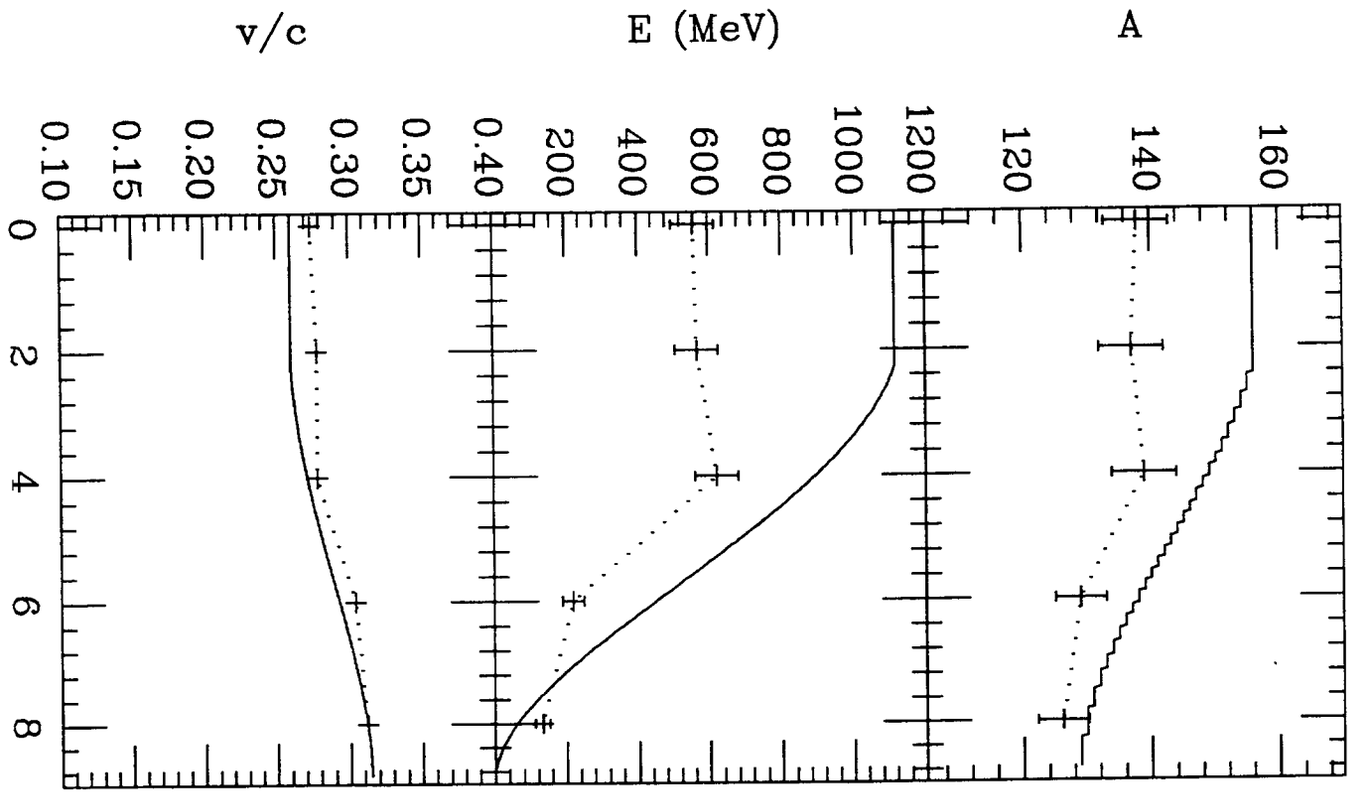
v/c
E (MeV)
A
0.10
0.15
0.20
0.25
0.30
0.35
0.40
200
400
600
800
1000
1200
120
140
160
0
2
4
6
8

Fig. 23

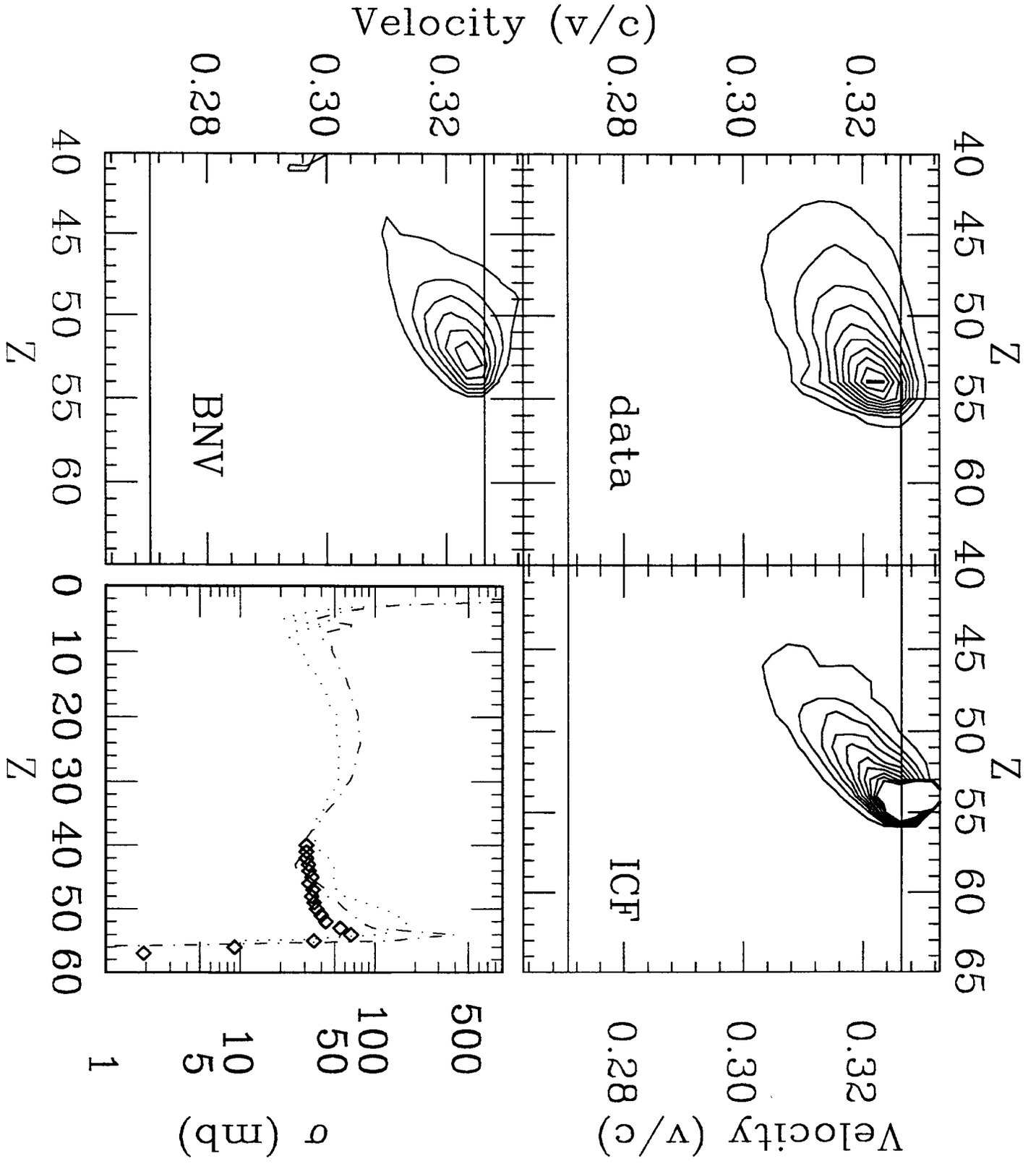
Velocity (v/c)
0.28
0.30
0.32
40 45 50 55 60 Z
BNV
data
ICF
0 10 20 30 40 50 60 Z
σ (mb)
1
5
10
50
100
500
Velocity (v/c)
0.28
0.30
0.32
40 45 50 55 60 65 Z

Fig. 24